

Bayesian Approaches to the Cosmic Dipole

Vasudev Mittal

*A dissertation submitted for the partial fulfilment of BS-MS dual degree
in Science*



Indian Institute of Science Education and Research, Mohali

April 26, 2024

Certificate of Examination

This is to certify that the dissertation titled **Bayesian approaches to the cosmic dipole** submitted by **Vasudev Mittal** (Reg. No. MS19004) for the partial fulfillment of BS-MS Dual Degree program of the Institute, has been examined by the thesis committee duly appointed by the Institute. The committee finds that the work done by the candidate is satisfactory and recommends that the report be accepted..

Prof. Kulinder Pal Singh

Prof. Jasjeet Singh Bagla

Dr. Pankaj Kushwaha

Prof. Kulinder Pal Singh
(Local Supervisor)

Prof. Geraint F. Lewis
(External Supervisor)

Dated: April 26, 2024

Declaration

The work presented in this dissertation has been carried out by me under the guidance of **Prof. Geraint F. Lewis** from **The University of Sydney** and **Prof. Kulinder Pal Singh** at the Indian Institute of Science Education and Research, Mohali.

This work has not been submitted in part or in full for a degree, a diploma, or a fellowship to any other university or institute. Whenever contributions of others are involved, every effort is made to indicate this clearly, with due acknowledgement of collaborative research and discussions. This thesis is a bonafide record of original work done by me and all sources listed within have been detailed in the bibliography.



Vasudev Mittal

(Candidate)

Dated: April 26, 2024

In my capacity as the supervisor of the candidates project work, I certify that the above statements by the candidate are true to the best of my knowledge.

Prof. Kulinder Pal Singh
(Local Supervisor)

Prof. Geraint F. Lewis
(External Supervisor)

Dated: April 26, 2024

Acknowledgements

First of all, I thank Prof. Geraint F. Lewis for his constant support and encouragement. His guidance has enabled me to learn a lot, focus on what is important, and explore different frontiers of the dipole anisotropy problem on my own. This work would not have materialized without his belief in my abilities. In addition to his insights into cosmology, he also taught me a lot about science popularization, bears, and Welsh culture. I thank Prof. Kulinder Pal Singh for his supervision and rigorous feedback. He encouraged me to work in dipole anisotropy and has acted as a pillar of support for me during the past two years. He also helped me in becoming a better person by giving me valuable lessons about life and human nature.

I thank Prof. Tara Murphy for sharing her expert opinion on radio galaxies. The radio galaxy paper became possible because of her insights. A special thanks goes to Prof. Jasjeet Bagla, Dr. Harvinder Jassal, Dr. Kinjalk Lochan, and Dr. Pankaj Kushwaha. They taught me the basics of astrophysics and cosmology both in and outside the classroom.

A big thanks to my friend and esteemed colleague, Mr. Oliver T. Oayda. The work presented in this thesis was done jointly by us during the past year. I thank my colleagues from The University of Sydney: Mr. Chengyi Wang, Mr. Eben Taylor, Ms. Huimin Qu, Ms. Nada Salama, Ms. Smrithi G. B., and Ms. Gargi Tyagi for teaching me new things and helping me during my stay in Australia.

Finally, I thank my father, Mr. Sukhdev Mittal, and mother, Dr. Alka Mittal, for their love and support all these years.

I acknowledge financial support from the DST-INSPIRE-SHE scholarship and The University of Sydney's internship program, which made this work possible.

**अखण्डमण्डलाकारं व्याप्तं येन चराचरम् ।
तत्पदं दर्शितं येन तस्मै श्रीगुरवे नमः ॥**

Salutations to my teachers who revealed to me that Truth, which is unfragmented, infinite, timeless divinity, and which pervades the entire universe – movable or unmovable.

Abstract

The Cosmological Principle asserts that the universe is isotropic and homogeneous on large scales and attributes the Cosmic Microwave Background (CMB) thermal dipole to our departure from the local Hubble flow. If this attribution is correct, then surveys of cosmological sources should show a similar dipole in their sky distribution. However, recent studies have found a disagreement between the kinematic expectations and the observed clustering dipole, with claims reaching well over 5σ ! This thesis aims to study this tension between the kinematic dipole and the matter dipoles.

The first part of this thesis is devoted to Bayesian analysis of the Quaia sample of quasars as a test of the cosmological principle. We test various hypotheses for the quasar distribution in Quaia, and find that selection effects contaminate the sample near the Galactic center. After masking these regions, we find that the Quaia matter dipole is relatively consistent with the CMB kinematic dipole. These results support the Cosmological Principle and the kinematic interpretation of the matter dipole.

The second part of this thesis intends to study the matter dipole in the NRAO VLA Sky Survey (NVSS) and the Rapid ASKAP Continuum Survey (RACS) radio galaxy catalogues. We find that local radio sources in both NVSS and RACS give a non-negligible contribution to the matter dipole signal. By proper consideration of these sources, the tension between CMB kinematic dipole and radio galaxy matter dipole is relaxed, and their consistency is favoured. Therefore, our joint analysis of both catalogues support the Cosmological Principle. However, the ‘clustering dipole’ in local sources appears to align with the kinematic dipole, which warrants further inquiry.

List of Figures

Introduction

1.1 CMB and CMB Thermal Dipole	4
1.2 Dipolar modulation of sky using E & B formula	5

Bayesian Statistics

2.1 Evidence calculation in nested sampling	11
---	----

Quaia quasars

3.1 Quaia catalogues	18
3.2 All-sky maps of selection effects	19
3.3 Selection function	20
3.4 Spectral index and source number counts	21
3.5 Kinematic dipole amplitudes	22
3.6 Reconstructed double dipole signal for a 30° mask	25
3.7 Inferred dipole parameters	26
3.8 Contamination in Quaia high	27

RACS and NVSS radio galaxies

4.1 RACS: source density vs flux & flux distribution	30
4.2 RACS(A) & RACS(B)	31
4.3 NVSS: source density vs flux & flux distribution	32
4.4 NVSS(A) & NVSS(B)	33
4.5 Corner plot for free dipole fit to individual catalogues	36
4.6 Corner plot for the joint RACS(B) and NVSS(B) analysis	37
4.7 All-sky projection of joint analysis of RACS(B) and NVSS(B)	37
4.8 Inferred dipole amplitude vs redshift of removed sources	38
4.9 Local sources contributing to clustering dipole.	39
4.10 All-sky projection of clustering dipoles.	40

List of Tables

Table of Bayes Factors for Quaia quasars

A.1	Quaia low, point-by-point likelihood	45
A.2	Quaia low, Poisson likelihood	45
A.3	Quaia high, point-by-point likelihood	46
A.4	Quaia high, Poisson likelihood	46

Disc masks for RACS and NVSS radio galaxies

B.1	Masked regions in RACS	47
B.2	Masked regions in NVSS	47

Summary of RACS and NVSS radio galaxies

C.1	RACS(A) and RACS(B) variants	48
C.2	NVSS(A) and NVSS(B) variants	48

Table of Bayes Factors for RACS and NVSS radio galaxies

D.1	RACS, individual analysis	49
D.2	NVSS, individual analysis	49
D.3	RACS(B) and NVSS(B), joint analysis	50

Contents

Abstract	V
List of Figures	VI
List of Tables	VII
1 Introduction	1
1.1 The Cosmological principle and FLRW paradigm	1
1.2 Number count dipole test	3
1.2.1 CMB kinematic dipole	3
1.2.2 Number count dipole	3
1.3 This thesis	7
1.3.1 Outline	7
2 Bayesian Statistics	9
2.1 Bayesian statistics	9
2.1.1 Bayes theorem	9
2.1.2 Nested sampling	10
2.2 Likelihood functions	12
2.2.1 Poisson Likelihood	12
2.2.2 Point-by-point analysis	13
2.2.3 Selection effects	13
2.3 Hypotheses under consideration	14
2.3.1 Monopole (null)	14
2.3.2 Dipole	14
2.3.3 Dipole pointing in CMB dipole direction	14

2.3.4	Dipole with CMB inferred velocity	15
2.3.5	CMB dipole	15
2.3.6	Double dipole	15
2.3.7	Quadrupole	16
3	Quaia quasars	17
3.1	Background	17
3.2	Catalogue Construction	18
3.2.1	Selection functions	18
3.3	Processing pipeline	19
3.3.1	Masking	19
3.3.2	Dipole amplitude expectation	20
3.3.3	Choice of priors	22
3.4	Results	23
3.4.1	Quaia Low	23
3.4.2	Quaia high	23
3.5	Discussion	24
3.5.1	Dominance of Double Dipole	24
3.5.2	Contamination in Quaia high	27
3.5.3	Dipole estimation for Quaia	28
3.6	Impact of priors on the results	28
4	NVSS and RACS radio galaxies	29
4.1	Background	29
4.2	Catalogue Preparation	30
4.2.1	RACS	30
4.2.2	NVSS	31
4.3	Processing pipeline	33
4.3.1	Dipole amplitude expectation	33
4.3.2	Likelihood function and choice of priors	34
4.4	Results	35
4.4.1	RACS	35
4.4.2	NVSS	35

4.4.3	Joint analysis: NVSS+RACS	35
4.5	Discussion	36
4.5.1	Effect of local clustering	36
4.5.2	Joint analysis of RACS and NVSS	41
4.6	Comparison with other studies	41
5	Summary and Concluding remarks	43
A	Table of Bayes Factors for Quaia quasars	45
B	Disc masks for RACS and NVSS radio galaxies	47
C	Summary of RACS and NVSS radio galaxies	48
D	Table of Bayes Factors for RACS and NVSS radio galaxies	49
Bibliography		51

Chapter 1

Introduction

1.1 The Cosmological principle and FLRW paradigm

The Cosmological Principle (CP) dictates that the universe is homogenous and isotropic at the large scales [Harrison 00, Milne 35]. First proposed by Newton in *Principia Mathematica* [Newton 87], the CP was subsequently adopted by Einstein in his static universe [Einstein 17]. Friedmann [Friedmann 22] and Lemaître [Lemaître 31] independently calculated solutions to Einstein's equations for a homogeneous and isotropic non-static universe. Robertson and Walker [Robertson 35] conclusively showed that the Friedmann-Lemaître-Robertson-Walker (FLRW) metric is the only possible solution obeying both homogeneity and isotropy. It is important to note that their proof was purely geometric unlike Friedmann and Lemaître's proof that was not tied to equations of general relativity. Since the main idea of this work is to put the CP to test, a brief discussion on how the CP forms the basis of FLRW metric and Friedmann equations is in order.

The CP¹ mandates that the universe should be a maximally symmetric manifold. Since cross-terms of the form $dtdx^i (i = 1, 2, 3)$ only appear due to strong gravitational environment, these terms are not expected to be present in the metric. Finally, g_{tt} should not depend on radial coordinates because all observers should measure the same coordinate time interval between any two events. The most general metric for an expanding universe, obeying these constraints is given by

$$ds^2 = -f(t)dt^2 + a^2(t)d\sigma^2 = -d\tilde{t}^2 + a^2(t)d\sigma^2 \quad (1.1)$$

where we have re-scaled our time coordinates in the final equation and have set $c = 1$ (we

¹This discussion is mostly based on my personal notes, but can be found in any standard cosmology textbook such as [Weinberg 08].

will refer to \tilde{t} as t from now on). Here the scale factor $a(t)$ cannot depend on r because that would violate homogeneity and, $d\sigma^2$ is the isotropic, maximally symmetric 3-space metric (γ_{ij}) defined as

$$d\sigma^2 = \gamma_{ij}dx^i dx^j = e^{2\beta(r)}dr^2 + r^2 d\Omega^2 \quad (1.2)$$

Furthermore, the maximal symmetry of γ_{ij} should imply that the 3-space Riemann and Ricci tensors of the form (K is gaussian curvature)

$$\tilde{R}_{ijkl} = K(\gamma_{ik}\gamma_{jl} - \gamma_{il}\gamma_{jk}) \Rightarrow \tilde{R}_{jl} = \gamma^{ia}\tilde{R}_{ijkl}|_{a=k} = 2K\gamma_{jl} \quad (1.3)$$

Substituting 1.2 in 1.3 and solving for β using \tilde{R}_{rr} gives

$$e^{-2\beta(r)} = 1 - Kr^2 \Rightarrow d\sigma^2 = \frac{dr^2}{1 - Kr^2} + r^2 d\Omega^2 \quad (1.4)$$

normalizing the amplitude of gaussian curvature by setting $k = \alpha K$, $k \in (-1, 0, 1)$, reparameterizing radial coordinates as $\tilde{r} = \sqrt{\alpha}r$ and substituting in 1.4, we get

$$ds^2 = -c^2 dt^2 + a^2(t) \left(\frac{dr^2}{1 - kr^2} + r^2 d\Omega^2 \right) \quad (1.5)$$

where we have reinstated c , absorbed α in $a(t)$ and have relabelled \tilde{r} as r . Clearly, the notion of homogeneity is vested in g_{tt} and a 's non-dependence on r and isotropy is vested in $r^2 d\Omega^2$, which is the line element for a 2-sphere. Substituting this metric into the Einstein's field equations gives the Friedmann equations

$$\begin{aligned} 2\frac{\ddot{a}}{a} + \frac{\dot{a}^2 + kc^2}{a^2} - \Lambda c^2 &= -\frac{8\pi G}{c^2} p \\ \frac{\dot{a}^2 + kc^2}{a^2} - \frac{\Lambda c^2}{3} &= \frac{8\pi G}{3c^2} \epsilon \end{aligned} \quad (1.6)$$

where p and ϵ are the pressure and energy density of vacuum, Λ is the cosmological constant.

Based on this framework, many important predictions related to origin, evolution and fate of our universe have been made. With the advent of precision cosmology, an increase in good quality data has resulted in acceptance of some, rejection of others and formulation of new predictions.

The above discussion shows that the CP forms the cornerstone of some of the most revolutionary ideas of past 100 years. Hence it is important to test this ansatz using cosmological observations. In an ideal situation, the CP and Λ -CDM model should account for all the cosmological observations, and any disagreement should be within statistically

acceptable limits. Any unexplained data with high statistical discrepancy would signal a breakdown of the framework, which will necessitate a reconsideration of the theories of relativistic cosmologies.

Although a plethora of tests are available for testing both homogeneity and isotropy (see [Kumar Aluri 23] for details), we narrow down our interest to testing the isotropy of the universe using the number count dipole test. Conceived by Ellis and Baldwin in 1984 [Ellis 84], it was first implemented by Blake and Wall in 2002 [Blake 02]. Recent results in this domain have shown a departure from the CP with a high statistical significance of 5.7σ [Dam 23, Secrest 22], which has brought this tension to the center stage of modern cosmology [Peebles 22]. A failure to relax this tension would signal a departure from the assumption of isotropy of the universe, which will point towards a breakdown of the CP and hence the Λ -CDM model.

This work intends to understand the genesis of the dipole anisotropy tension and make an attempt to relax it. In order to complete this task, the need is to understand the dipole anisotropy in detail. This chapter is dedicated to discussing the dipole anisotropy and is structured as follows. In Section 1.2, we discuss the CMB kinematic dipole, and the number count dipole test in detail. We also discuss some modifications to the number count dipole test that are implemented in our analysis. In Section 1.3, we give an outline for this thesis.

1.2 Number count dipole test

1.2.1 CMB kinematic dipole

Cosmic Microwave Background (CMB) is a relic radiation filling the entire universe. Formed by photons that decoupled from matter at a redshift of $z \approx 1100$, this background was generated at the time of matter-photon decoupling. Small scale temperature fluctuations in CMB are of the order of $10\mu\text{K}$, and are thought to be the progenitors of large scale structure in the late universe. This smooth temperature map is imprinted with a dominant dipole anisotropy of the order of 1mK . It is interpreted as arising out of our local group's motion towards $(l, b) = (264^\circ.021, 48^\circ.253)$ with a speed of $369.82 \pm 0.11\text{km/s}$ [Planck Collaboration 20]. Figure 1.1 shows both the CMB temperature fluctuations (top panel) and the dipole anisotropy (bottom panel). The dark region running through the bottom panel is the galactic plane.

1.2.2 Number count dipole

If the kinematic interpretation of CMB dipole anisotropy is correct, then surveys of other cosmological distant probes should show a similar dipolar modulation in their distribu-

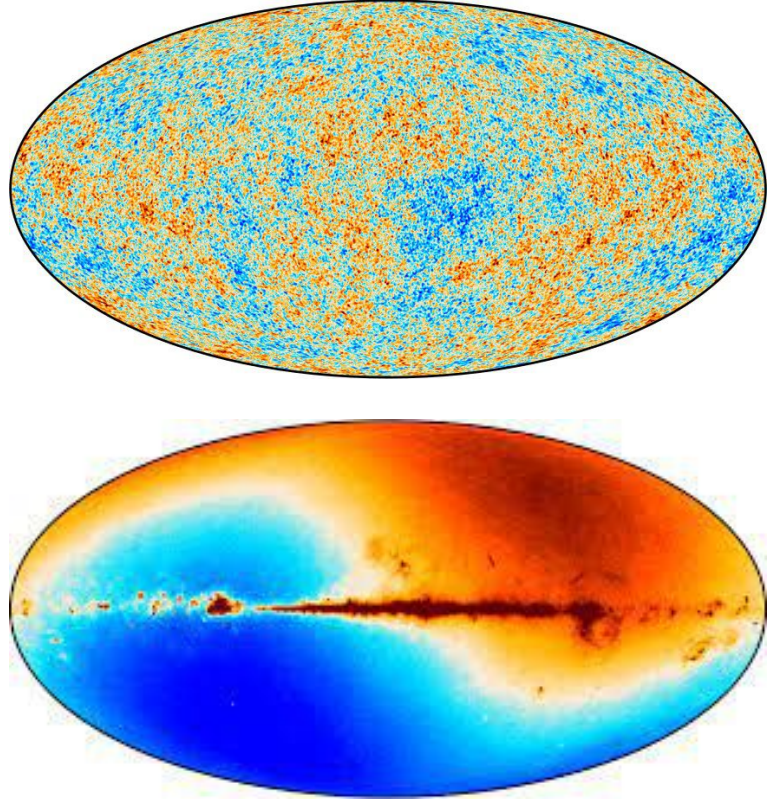


Figure 1.1: CMB fluctuations (top panel) are seen after subtracting a dominant dipole anisotropy (bottom panel). The dark region running through the bottom panel is the galactic plane which is usually removed during processing; picture credits: [BeyondPLANCK Collaboration](#)

tion throughout the sky. Ellis and Baldwin [[Ellis 84](#)] calculated the modulation in number counts due to our peculiar motion. They made the following assumptions:

1. The observer is moving with a velocity $v \ll c$ with respect to a homogeneous and isotropic background.
2. The spectral energy distribution for sources has a power law dependence on frequency $S_f \propto f^{-\alpha}$ for spectral index α and frequency f .
3. The cumulative number counts are a function of flux density S i.e. $N(> S) \propto S^{-x}$.
4. There are $\mathcal{O}(10^5)$ sources distributed throughout the sky.
5. The mean redshift of the sources is $z \approx 1$.

Under these assumptions, relativistic aberration and Doppler boosting will modify an isotropic distribution of sources throughout the sky. Upto a leading order, this effect will induce a dipole anisotropy of the form

$$\frac{\Delta N}{N} = \mathbf{D} \cdot \hat{\mathbf{n}} = [2 + x(1 + \alpha)] \frac{\mathbf{v}}{c} \cdot \hat{\mathbf{n}}. \quad (1.7)$$

where N denotes the number of sources in direction \hat{n} , and $\frac{\Delta N}{N}$ gives the relative modulation. The amplitude of the dipole is theorised to be

$$\mathcal{D} = [2 + x(1 + \alpha)] \frac{v}{c}. \quad (1.8)$$

This modulation is dubbed as the matter dipole and is visualised in Figure 1.2 for a syn-

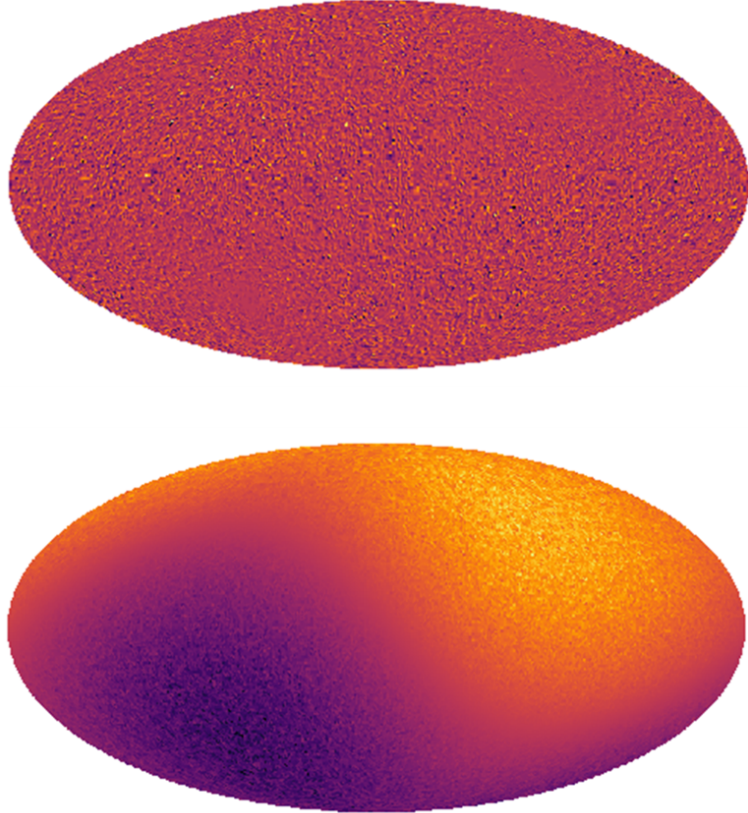


Figure 1.2: An isotropic synthetic sky (top panel) modulated to show a dipole anisotropy using Ellis and Baldwin formula with a kinematic velocity.

thetic catalogue. There, the top panel gives an isotropic sky, and which when modulated for some fixed values of x and α , gives the dipolar modulation shown in the bottom panel. Before implementing this test on any catalogue, there are some important factors that we need to consider. We discuss these in detail below.

Catalogue Binning

Ellis and Baldwin test necessitates the need to divide the sky into regions of roughly equal area. Although, there are many ways to perform this task, in this work we rely on HEALPY, a PYTHON library utilizing the HEALPix [Górski 05, Zonca 19] pixelization, which divides the sky into equal-area patches.

We use $N_{side} = 64$, with a ring ordering, that generates a total of 49152 pixels. The

choice of N_{side} is determined by the fact that for a robust statistical analysis of number count fluctuations, the uncertainty in number counts due to shot noise should be less than the mean number count for the catalogue. The number of sources in each pixel were summed to generate a means to analyse the number density variations as a function of sky positions.

Modified dipole amplitude expectation

Efforts have been made to relax some of the assumptions of Ellis and Baldwin test. Studies like [Dalang 22], have pointed out the need to relax the implicit assumption of redshift independence of x and α . Other works such as [Tiwari 16] have point need to have high-redshift sources, in order to avoid the problem of clustering dipole, something which we have found in our analysis as well.

Another issue is the cumulative source count's power law dependence on flux. In previous analysis of all-sky datasets such as radio galaxies and quasars, the source count distribution has been assumed to be a power law fit S^{-x} . While this is true for radio galaxies, in many cases like quasars, a visual inspection of the logarithmic scale graph of flux vs integrated source count will reveal that the fit is not a straight line (which is equivalent to power-law on a linear scale). Previous works have overlooked this fact: they have either assumed a straight line (see e.g. [Secrest 21]), or have used piece-wise straight line fit (see for e.g. [Singal 23]). But these are only approximations, and hence there is a need to develop a better method for determination of expected kinematic dipole amplitude for a dataset. In [Mittal 24], we have developed an approach to do away with this simplification. The following discussion highlights this approach.

If a population of sources and corresponding fluxes are observed, the expectation is the enhancement of number counts in forward direction and diminution in backward direction; with the sources becoming brighter and fainter respectively and crowding along the line of motion. These effects are the underlying assumption of $N(> S) \propto S^{-x}$ by [Ellis 84]. Thus, the following strategy was adopted:

1. First compute the number of sources n_i , with flux greater than S_0 (a limiting flux density).
2. For the k -th source with observed flux S_k , doppler boost the flux to $S_k \delta^{1+\alpha}$ where $\delta = \gamma(1 + \frac{v}{c} \cos \theta)$ and γ is the Lorentz factor.
3. Compute the number of boosted fluxes greater than some limiting flux density and multiply this by δ^2 , to account for relativistic aberration. This number count is labelled as n_b .

4. Using the above results, the expected dipole amplitude is

$$\mathcal{D} = \frac{n_b - n_i}{n_i}. \quad (1.9)$$

Here, we fix S_0 to a value near catalogue's flux limit and consider the line of motion measurement it $\theta = 0$. This method is useful for a non-power-law integrated flux count distribution, and we will study its implementation in Chapter 3.

Choice of statistics

Previous studies of dipole anisotropy in quasars and radio galaxies rely on frequentist statistics, and estimators are used for estimating the dipole from the dataset. However, it is well known that estimators suffer from bias, which might be due to the assumptions used in creating them, insufficient sky coverage, or catalogue properties. Characterising estimator bias is a challenging and often messy task, and sometimes almost half of the paper has been devoted to studying the estimators being used. In this work, we turn away from estimators and instead work with the Bayesian statistics. First utilised by [Dam 23] in dipole studies, Bayesian statistics has revolutionised the field as they remove the bias characterisation from the picture. Bayesian statistics have also been utilised by recent works such as [Wagenveld 23, Mittal 24] and have paved way for studying the dipole anisotropy with a fresh perspective.

1.3 This thesis

Over the course of this introduction, we have learnt how the CP forms the basis of Λ -CDM framework, and hence acts as the backbone of modern cosmology. Given its status as the cornerstone of the domain, it is important to put it to test. Although, a suite of tests are available (see [Kumar Aluri 23] for a detailed discussion), yet the focus of this thesis is to test the assumption of isotropy by checking for consistency between matter and kinematic dipoles. We will study this dipole anisotropy tension in quasars and radio galaxies by using Bayesian statistics.

1.3.1 Outline

This thesis is structured as follows:

Chapter 2 discusses Bayesian statistics in detail. We motivates the choice of Bayesian statistics for fitting a model to the data and testing hypotheses, looking at different levels of inferences along the way. This is followed by a discussion on calculating the marginal

likelihoods for different hypotheses using the nested sampling algorithm. Next, we discuss our choice of likelihood functions and how selection effects in quasars modify them. We end the chapter by a discussion on various hypotheses that have been tested on the dataset.

In Chapter 3, we analyse the dipole anisotropy in quasars. We work with a new quasar sample and process the catalogues to remove the density fluctuations and motivate our choice of priors for analysis. Then we present our results and discuss their interpretation in detail, ending with analysing the impact of modifying our priors on the results. This chapter is complemented by the Appendix A, where we have presented our tables of Bayes factors for different hypotheses and likelihoods.

Chapter 4, is devoted to study of the dipole tension in all-sky surveys of radio galaxies. We perform a joint analysis two radio galaxy catalogues, and study impact of local sources on the inferred dipole amplitude. Then we present our results and discuss their interpretation, ending with a comparison of our analysis with previous studies. This chapter is complemented by the Appendices B, C and, D.

In Chapter 5, we summarise our main findings and discuss possible work trajectories for future.

Chapter 2

Bayesian Statistics

2.1 Bayesian statistics

The choice of Bayesian statistics is motivated by two major factors:

1. Firstly, probability in Bayesian statistics is a degree of belief assigned to a particular hypothesis, unlike frequentist case where it is a quantitative value assigned to a result. This feature makes it suitable for hypothesis comparison, and leaves some scope for unknown variables in our problem.
2. Bayesian statistics makes use of previous knowledge about the problem through priors. This makes it a powerful statistical tool, as it allows us to incorporate already available information into the analysis, hence increasing the reliability of our results.

2.1.1 Bayes theorem

Bayesian statistics works on two levels of inference. At the first level, it is an optimization algorithm where a model's parameters are optimized and their posterior distribution is recovered. This is achieved by solving the Bayes theorem

$$P(\Theta|\mathbf{D}, M) = \frac{\mathcal{L}(\mathbf{D}|\Theta, M)\pi(\Theta|M)}{\mathcal{Z}(\mathbf{D}|M)}. \quad (2.1)$$

and determination of the posterior distribution $P(\Theta|\mathbf{D}, M)$ of model M 's parameters Θ by fitting it to a dataset \mathbf{D} . Here \mathcal{L} is the likelihood of observing the data \mathbf{D} if the model M with free parameters Θ is assumed to be true. π encodes our prior knowledge about Θ and \mathcal{Z} is a normalization factor which is dubbed as the evidence or marginal likelihood and is given as the integral of likelihood over the parameter space Ω_Θ :

$$\mathcal{Z} = \int_{\Omega_\Theta} \mathcal{L}(\Theta)\pi(\Theta) d\Theta \quad (2.2)$$

At second level, the evidence is no longer a normalization factor, rather it is used to rank competing hypotheses by calculating Bayes factors, which are just ratios of marginal likelihoods for competing models. Put it differently, the relative support for models M_1 and M_2 is determined by calculating

$$\ln B_{12} = \ln \mathcal{Z}_1 - \ln \mathcal{Z}_2 \quad (2.3)$$

where B is the Bayes factor. Since \mathcal{Z} are extremely small values, it is beneficial to work in natural logarithms. From now on, any reference to the Bayes factor will correspond to its natural logarithm. In this formalism, it is quite easy to determine the relative support for different hypotheses. A positive value for $\ln B_{12}$ will imply that M_1 is preferred over M_2 , a negative value will imply vice-versa, and a 0 value will imply equal support for both hypotheses.

Given the nature of \mathcal{Z} , models that have excessive parameters are disfavoured because they waste the parameter space. Following the arguments of [Mackay 03], the evidence can be approximated by

$$\mathcal{Z} \approx \mathcal{L}(\Theta_{\text{MP}}) \frac{\Delta\Theta}{\Delta^0\Theta} \quad (2.4)$$

where $\mathcal{L}(\Theta_{\text{MP}})$ is the likelihood value at the optimal parameter values and $\frac{\Delta\Theta}{\Delta^0\Theta}$ is the Occam factor: the ratio of the peak in likelihood to the width of prior. Occam's factor penalizes those models that waste parameter space and only have a high likelihood in a small region.

The above discussion shows the importance of evidence in comparing competing hypotheses and ranking them. Hence, we need an efficient way to calculate \mathcal{Z} . One such algorithm is nested sampling, which has been discussed below.

2.1.2 Nested sampling

A major issue with Bayesian statistics is the calculation of evidence integral. In most cases, it is not feasible to calculate it analytically and is numerically expensive. Fortunately, advances in computational methods have made this easy. In this work, we utilize the nested sampling (NS) algorithm [Skilling 04, Skilling 06]. NS works by computing evidence as the primary quantity and evaluates the posterior distribution of the free parameters for a model as a ‘subsidiary element’ [Skilling 04].

NS recasts the evidence integral from parameter space θ to the $\xi(\lambda)$ space. Here, $\xi(\lambda)$ gives the amount of prior $\pi(\theta)$ with likelihood $\mathcal{L}(\theta)$ larger than some value λ .

$$\xi(\lambda) = \int_{\mathcal{L}(\theta) > \lambda} \pi(\theta) d\theta \quad (2.5)$$

Here, $\xi \in [0, 1]$ and its differential is defined as

$$d\xi = \pi(\theta)d\theta \quad (2.6)$$

In this formalism, the \mathcal{L} is the area under the $\mathcal{L} - \xi$ curve (as shown in Fig. 2.1, left)

$$\mathcal{L} = \int \mathcal{L}(\theta) \pi(\theta) d\theta = \int_0^1 \mathcal{L}(\xi) d\xi \quad (2.7)$$

and the posterior distribution is obtained as a byproduct i.e. $P(\xi)$ becomes

$$P(\xi) = \frac{\mathcal{L}(\xi)}{\mathcal{L}} \quad (2.8)$$

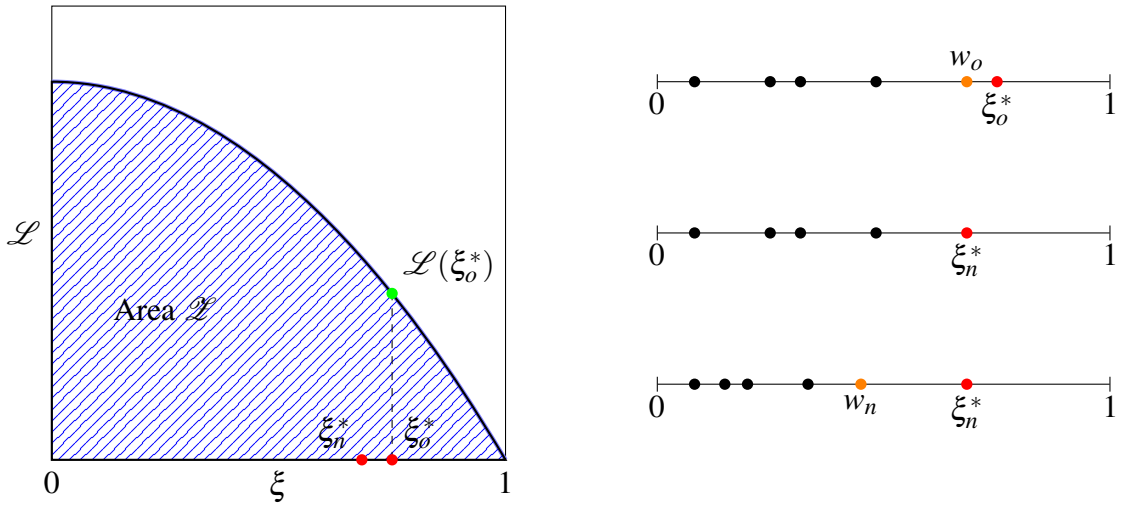


Figure 2.1: (a) Likelihood function with area \mathcal{L} . The figure is not to scale since most of the area is present in proximity of a small value of ξ ; (b) Nested sampling works by sampling for a new worst object inside the shrunken domain of the current worst object.

In this formalism, the evidence integral is calculated in the following fashion (refer to right side of Fig. 2.1)

1. Firstly, a finite number of random points (say n points) are selected on the ξ axis. The largest of these points is labelled as ξ_o^* , the second largest point is labelled as w_o and corresponding \mathcal{L} value $\mathcal{L}(\xi_o^*)$ is noted.
2. In the next step, w_o is labelled as ξ_n^* , and another random set of $n - 1$ ξ values between 0 and ξ_n^* are selected, and the largest value of this set is labelled as w_n .
3. Step 1 and 2 are repeated by relabelling ξ_n^* and w_n from step 2 as the new ξ_o^* and w_o for step 1. Since successive values of ξ are sampled in their predecessor's nesting space, the algorithm is called nested sampling.

4. Finally, the value of \mathcal{L} is calculated by addition of the product of $\mathcal{L}(\xi_o^*)$ with the difference of ξ_o^* and ξ_n^* of each step i.e.

$$\mathcal{L} = \sum_k \mathcal{L}(\xi_{o,k}^*)(\xi_{n,k}^* - \xi_{o,k}^*) \quad (2.9)$$

2.2 Likelihood functions

Armed with a tool to compute the evidence and posterior distributions, its time to turn towards formulating our problem in statistical terminology. The first step in performing Bayesian analysis of any dataset is to construct the likelihood function \mathcal{L} . In this work, we will consider two independent approaches for constructing \mathcal{L} . While both the approaches have same underlying assumptions, yet their different formulation gives scope for cross-checking the results. We will study the likelihood functions in a model-invariant fashion and discuss their alteration for different hypothesis as we proceed further. Due to the nature of quasar catalogue, it is necessary to take selection effects into account. This modification is discussed towards the end of this section.

2.2.1 Poisson Likelihood

This approach (used in [Dam 23]) relies on identifying the sky pixelization as a Poisson point process, where number density variations across pixels are explained by using an intrinsic signal and a shot noise. Shot noise necessitates association of number density in each pixel with a Poisson process, which means that the occupancy in each pixel is a random value sampled from a Poisson distribution. The intrinsic signal is hypothesis dependent, so it can be a monopole, dipole or something else. This identification associates Possion distribution's rate parameter with the pixel number density. So, the probability P of observing N_i sources in the i -th pixel is written as

$$P(N_i | \hat{\mathbf{p}}_i) = \frac{\lambda_i^{N_i} e^{-\lambda_i}}{N_i!} \quad (2.10)$$

where λ_i is i -th pixel's rate parameter and $\hat{\mathbf{p}}_i$ is the unit vector pointing towards that pixel. As discussed above, the expected number density for the i -th pixel is $E[N_i(\hat{\mathbf{p}}_i)] = \lambda_i$. If we associate each pixel with a similar likelihood, then the net likelihood for the whole sky will be the product of Poisson distributions associated with each pixel. For ease of calculations, the net likelihood is usually defined in terms of logarithm. Hence for a total of n_{pix} pixels, net likelihood \mathcal{L} is

$$\ln \mathcal{L} = \sum_{i=1}^{n_{pix}} \ln P(N_i | \Theta) \quad (2.11)$$

2.2.2 Point-by-point analysis

The second approach relies on examining each source individually, as opposed to studying them in a bunch. This means that the net likelihood will be a product of all the points, hence the name ‘Point-by-point’. Although this approach is efficient, yet due to large number of data-points, its computationally expensive and time consuming. These issues are bypassed by pixelating the sky to simplify calculations, hence assigning same probability to all points within a given pixel. It should be noted that this approach is not new. In fact, it was used by [Conn 11, Conn 12] for distance determination using the tip of red giant branch for a sparsely populated stellar system. Let f_i be the model dependent anticipated signal at i -th pixel. If each source is examined individually, then the distribution associating each point with a location dependent probability is proportional to f_i . Thus, for a pixel with N_i sources, the net probability is $\propto f_i^{N_i}$. For normalization, we need to take the effect of masking into account, hence the normalization should be done over all the unmasked pixels, so

$$\hat{f}_i = \frac{f_i}{\sum_{i=1}^{n_{\text{pix.}}} f_i}. \quad (2.12)$$

This implies that logarithm of net likelihood function is just

$$\ln \mathcal{L} = \sum_{i=1}^{n_{\text{pix.}}} N_i \ln \hat{f}_i. \quad (2.13)$$

In principle, both Poissonian and point-by-point likelihoods should give consistent results, since they have the same underlying effect. This claim is confirmed in Chapter 3, where both approaches give similar Bayes factors.

2.2.3 Selection effects

The quasar catalogue analysed by us comes with a selection function which associates a probability with each pixel. In addition to variations due to underlying signal and statistical fluctuations, the selection function gives an extra modulation to the pixel number density. The underlying reason for inclusion of this selection function is discussed in Chapter 3. Hence, inclusion of these selection effects is important for testing the assumption of isotropy. This inclusion is achieved by attenuation of the rate parameter λ_i or anticipated signal f_i with the value of selection function s_i at the i -th pixel.

Stated differently, this changes Poissonian probability distribution to

$$P(N_i | \hat{\mathbf{p}}_i) = \frac{(\lambda_i \times s_i)^{N_i} e^{-\lambda_i \times s_i}}{N_i!} \quad (2.14)$$

while the corresponding expectation value is modulated to $E[N_i(\hat{\mathbf{p}}_i)] = \lambda_i \times s_i$. On the other hand, the normalized anticipated signal is modulated to

$$\hat{f}_i = \frac{s_i \times f_i}{\sum_{i=1}^{n_{\text{pix}}} s_i \times f_i}. \quad (2.15)$$

With the likelihood functions defined properly, it is necessary to define the model dependent terms λ_i and f_i by defining our hypotheses.

2.3 Hypotheses under consideration

2.3.1 Monopole (null)

Let's assume that the distribution of sources is isotropic in our (observer) frame. In such a situation, the anticipated signal is a monopole, with each pixel having a mean number density \bar{N} . Hence, the expected signal for the Poissonian likelihood is

$$E[N_i(\hat{\mathbf{p}}_i)] = \lambda_i = \bar{N}. \quad (2.16)$$

On the other hand, the anticipated signal for point-by-point analysis is set to 1 i.e. $f_i = 1$. This is our null hypothesis for both quasars and radio galaxies. The parameter space is $\Theta_{\text{Pos.}} = \{\bar{N}\}$ for Poissonian likelihood and $\Theta_{\text{P}\times\text{P}} = \emptyset$ for point-by-point likelihood.

2.3.2 Dipole

Let's introduce \mathbf{D} , a vector pointing in direction of intrinsic dipole signal, with magnitude equal to the inferred dipole. Then, the anticipated number count is given by [Dam 23]

$$E[N_i(\hat{\mathbf{p}}_i)] = \lambda_i = \bar{N}(1 + \mathcal{D} \cos \theta_i) \quad (2.17)$$

where \mathcal{D} is the inferred dipole amplitude and θ_i is the directional offset between pixel vector and inferred dipole direction. The parameter space is given by $\Theta_{\text{Pos.}} = \{\bar{N}, \mathcal{D}, l, b\}$, where l and b specify the dipole direction in galactic coordinates. For point-by-point analysis, we have $f_i = 1 + \mathcal{D} \cos \theta_i$, and $\Theta_{\text{P}\times\text{P}} = \{\mathcal{D}, l, b\}$.

2.3.3 Dipole pointing in CMB dipole direction

For verification of kinematic interpretation of the cosmic dipole, we fix certain dipole parameters to their CMB determined values and infer the rest from the data. This allows for comparison of marginal likelihoods in cases where kinematic interpretation is assumed

with cases where it is not assumed. First, we fixed $(l, b) = (264^\circ 0.21, 48^\circ 253)$ in dipole hypothesis and allow its amplitude to vary. This reduces parameter space to $\Theta_{\text{Pos.}} = \{\bar{N}, \mathcal{D}\}$ and $\Theta_{\text{P} \times \text{P}} = \{\mathcal{D}\}$

2.3.4 Dipole with CMB inferred velocity

Conversely, we can fix the dipole amplitude to a value that is dependent on catalogue parameter and CMB velocity. The details of dipole amplitude determination have been discussed in Chapter 1 in detail. The specific details for each catalogue are discussed in their respective chapters. The parameter space in this case is given by $\Theta_{\text{Pos.}} = \{\bar{N}, l, b\}$ and $\Theta_{\text{P} \times \text{P}} = \{l, b\}$, while \mathcal{D} is pre-determined.

2.3.5 CMB dipole

We can also align the dipole in equation 2.17 with the CMB dipole. Thus, the \mathcal{D} will be fixed to its expectation value, while l and b will be fixed to their CMB values. This will serve as a benchmark for comparison of the inferred dipole with the CMB dipole. The parameter space in this case is given by $\Theta_{\text{Pos.}} = \{\bar{N}\}$ and $\Theta_{\text{P} \times \text{P}} = \emptyset$

2.3.6 Double dipole

In case of quasars, we check for the presence of a double dipole as well. This is motivated by the over-density region present above the galactic center in our quasar catalogue. The assumption here is that the two dipoles were generated at different times due to different reasons. While the first one was generated due to observer's motion, the second one adds another modulation on top of an intrinsic modulation, which warrants the use of a scaling operation for determining the net modulation. Thus the net modulation will be a multiplication of two individual modulations, and the expectation value for Poissonian likelihood will be

$$E[N_i(\hat{\mathbf{p}}_i)] = \lambda_i = \bar{N}[(1 + \mathbf{D}_1 \cdot \hat{\mathbf{p}}_i) \times (1 + \mathbf{D}_2 \cdot \hat{\mathbf{p}}_i)] \quad (2.18)$$

and $f_i = (1 + \mathbf{D}_1 \cdot \hat{\mathbf{p}}_i) \times (1 + \mathbf{D}_2 \cdot \hat{\mathbf{p}}_i)$ for the point-by-point analysis. The parameter space is given by $\Theta_{\text{Pos.}} = \{\bar{N}, \mathcal{D}_1, l_1, b_1, \mathcal{D}_2, l_2, b_2\}$ and $\Theta_{\text{P} \times \text{P}} = \{\mathcal{D}_1, l_1, b_1, \mathcal{D}_2, l_2, b_2\}$. Even if the assumption of double modulation is incorrect, Bayesian statistics will balance out the model's complexity and its explanatory power, which can offer additional insights into the quasar sample.

2.3.7 Quadrupole

For completeness, we will also test for an underlying quadrupole signal in case of quasar catalogue. Quadrupole signal is just a special case of the double dipole with $\mathbf{D}_1 \cdot \hat{\mathbf{p}}_i = -\mathbf{D}_2 \cdot \hat{\mathbf{p}}_i$ in equation (2.18), and offers insights into the nature of density fluctuations in the quasar catalogue. For Poissonian statistics, the expectation value for i -th pixel is

$$E[N_i(\hat{\mathbf{p}}_i)] = \lambda_i = \bar{N}(1 + \tilde{\mathcal{D}} \cos^2 \theta_i). \quad (2.19)$$

while the anticipated signal is $f_i = (1 + \tilde{\mathcal{D}} \cos^2 \theta_i)$. The parameter space is given by $\Theta_{\text{Pois.}} = \{\bar{N}, \tilde{\mathcal{D}}, l, b\}$ and $\Theta_{\text{P} \times \text{P}} = \{\tilde{\mathcal{D}}, l, b\}$ respectively.

Having defined the likelihoods and hypotheses, we now turn to apply them to various datasets and calculate the cosmic dipole. The next chapter is dedicated to dipole determination from quasars using a recently released quasar dataset. In this work, we have utilised DYNESTY [Speagle 20], a PYTHON package implementing nested sampling algorithm.

Chapter 3

Quaia quasars

3.1 Background

The number count dipole in quasars was first calculated in [Secrest 21], where it was shown that [Ellis 84] method is extendable to determine the matter dipole in quasar samples. The authors studied the matter dipole in CatWISE2020 [Marocco 21] quasar sample, using the least square estimator. They reported the presence of a matter dipole which was twice as large as the CMB dipole (with 4.9σ statistical significance). This result was supported by an independent analysis of CatWISE2020 in [Kothari 22]. The CatWISE result, taken together with a joint analysis of radio galaxy and quasar sample in [Secrest 22], has presented one of the more significant challenges to the CP in recent times. Independent of this, [Singal 21] utilised a sample of 0.28 million quasars and reported a matter dipole with excess magnitude as compared to CMB dipole. These results rely primarily on frequentist statistics, and are sensitive to the choice of estimator being used. However, [Dam 23] performed a Bayesian analysis of CatWISE2020 and reported the presence of an anomalously large dipole (with 5.7σ statistical significance), hence confirming the result of [Secrest 21].

If there is indeed a tension between CMB kinematic and quasar matter dipole, then, a closer inspection is needed. Ideally, calculating the matter dipole in an independent quasar sample can give deep insight into this tension. This chapter is dedicated to studying matter dipole in quasar distribution. We calculate the matter dipole in recently released Quaia catalogue [Storey-Fisher 23], and use Bayesian statistics to understand whether the inferred matter dipole is consistent with the kinematic dipole. *The work presented here has been published in MNRAS [Mittal 24].*

3.2 Catalogue Construction

The Quaia quasar catalogue [Storey-Fisher 23] is constructed from quasars observed by the Gaia [Gaia Collaboration 16] and listed in Gaia DR3 were selected [Gaia Collaboration 23a, Gaia Collaboration 23b]. The complete DR3 dataset of 6649162 quasars was used to construct the catalogue.

First, all sources with valid G , BP and RP band photo-metric magnitudes were selected. These were then cross-matched with WISE catalogue [Wright 10] using unWISE reprocessing to get information in infrared bands W_1 and W_2 . To remove sources with high proper motion, all candidates with $\mu > 10^{0.4(G-18.5)}$ mas/yr were removed. Then four color cuts: $W_1 - W_2 > 0.4$ (to remove stars), $G - W_1 > 2.15$ (to remove other stellar contaminants), $BP - G > (-0.3)$ (to remove galaxy contaminants) and $G - W_1 + 1.2(W_1 - W_2) > 0.3$ (to remove Magellanic clouds) were imposed.

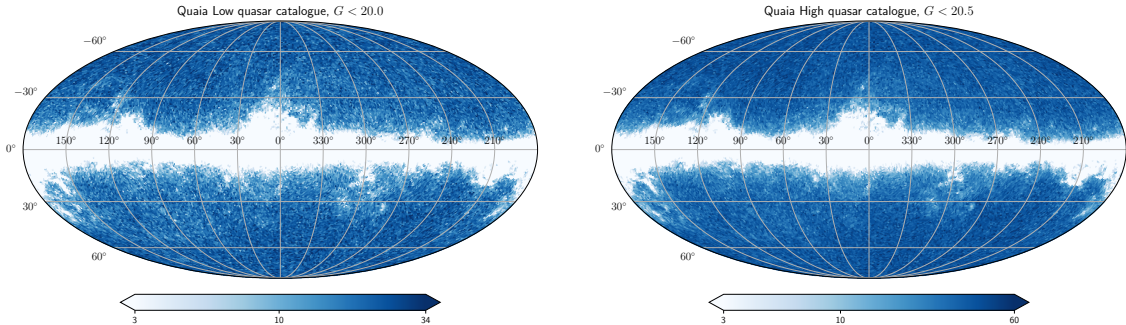


Figure 3.1: Visualization of the Quaia catalogues, in galactic coordinates, with Quaia low in left and Quaia high in right. Note that these are the raw catalogue prior to any additional masking or processing and they have an absence of sources near the galactic plane (white) primarily due to dust absorption. Color bar indicates the number of sources per HEALPixel

Finally, a $G < 20.5$ magnitude cut was imposed to reduce edge effects in redshift estimation. This gave the ‘Quaia high’ quasar catalogue (shown in right image of Fig. 3.1). Finally, the authors noted that deeper magnitudes compromised the sample purity and measurement precision, so an additional cut of $G < 20.0$ was imposed to construct the ‘Quaia low’ quasar catalogue (shown in left image of Fig. 3.1).

3.2.1 Selection functions

Despite removing most of the contamination, some outstanding selection effects are still present in the catalogues. To mitigate these, a selection function map was created by the authors to account for extinction due to dust, Gaia’s scanning pattern and stellar density. This information was taken from four maps which are shown in Fig. 3.2 (clockwise from

(top left): dust extinction map, stellar distribution map from Gaia, Gaia’s M_{10} map which encodes its scanning law and source crowding and a separate Magellanic cloud map constructed from the stellar distribution map.

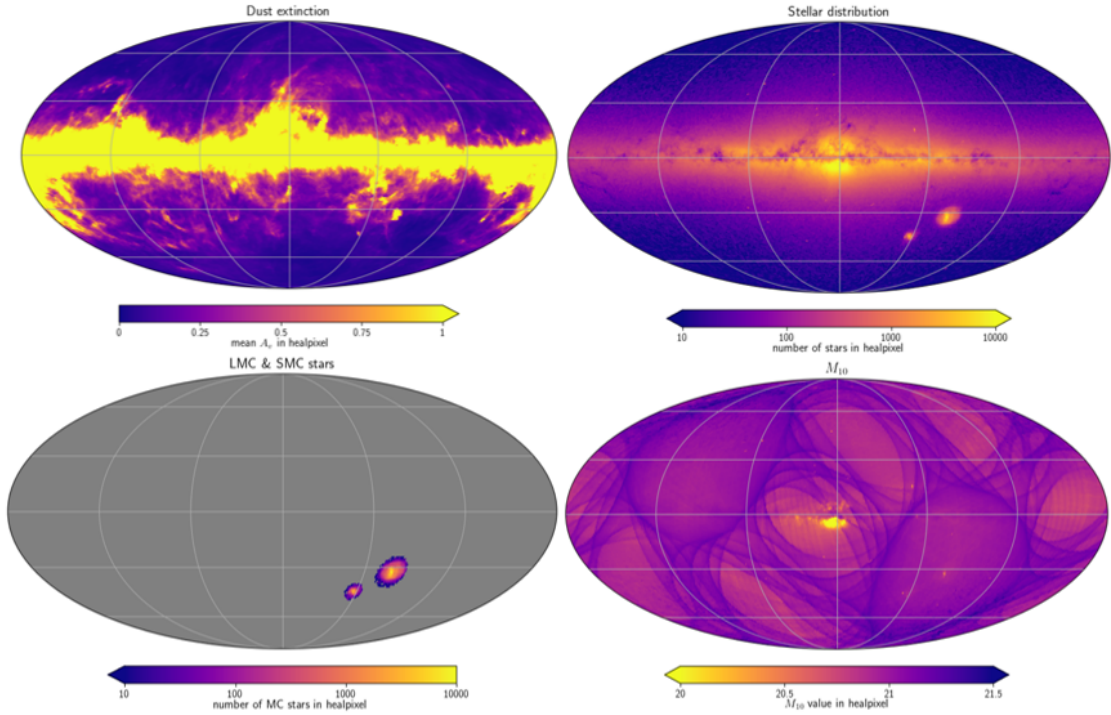


Figure 3.2: The raw Quaia catalogue had some outstanding selection effects as shown here: (a) dust extinction, (b) galactic stellar distribution, (c) Gaia M_{10} , and (d) large and small Magellanic clouds.

This data is combined using a Gaussian process, resulting in a probability map which is then scaled to individual catalogues. The output are two selection function maps, one each for Quaia low and Quaia high. The maps are shown in Fig. 3.3.

3.3 Processing pipeline

3.3.1 Masking

As noted by [Storey-Fisher 23], the selection function is not modelled correctly near the galactic plane. We find that near the galactic center, the selection function under-predicts the data, as there is an over-density near $(l, b) \approx (0^\circ, 30^\circ)$. On the other hand, around the galactic plane, the selection function over-predicts the data, as there is an under-density region stretching from about $l = 120^\circ$ to $l = 240^\circ$, along the galactic plane. This is in line with the findings of Quaia authors, as observed number counts N_i are scaled to predicted number counts \bar{N}_i by a division with the value of selection function s_i i.e. $\bar{N}_i = N_i / s_i$.

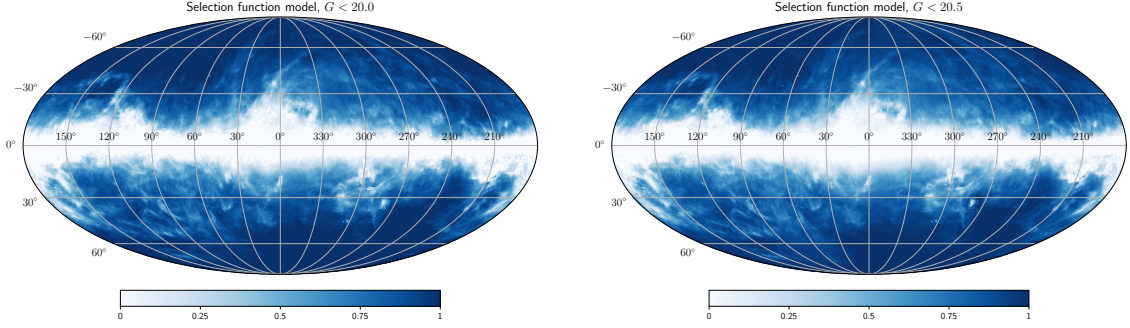


Figure 3.3: The selection function provided for both the Quaia catalogues. Color bar indicates the probability of source detection associated with each pixel.

In order to mitigate this issue, we adopt the advice made by Quaia authors and mask the Galactic plane with a series of increasing galactic plane masks. We examine the effects of $|b| < 10^\circ, 20^\circ, 30^\circ$ and 40° masks on the inferred dipole amplitude. Although, the 30° mask removes most of the problematic region, yet the probability of some density fluctuations not being removed (especially around the edge of the mask) is not zero. To address this issue, we additionally construct a 30^* mask, which is a combination of a $|b| < 30^\circ$ mask with a 4sr circular mask centered at the galactic center $(l^\circ, b^\circ) = (0, 0)$ and analyze that in conjunction with our other galactic plane masks.

3.3.2 Dipole amplitude expectation

In order to test our kinematic hypotheses, it is important to calculate the expected dipole amplitude for a CMB inferred motion and compare it with the recovered dipole amplitude. Ideally, this would require a knowledge of x and α , which will be used to calculate the dipole amplitude together with a velocity of $v \approx 370 \text{ km s}^{-1}$. The following discussion elaborates on these calculations.

Spectral index

Following the footsteps of Ellis and Baldwin, we assume that each source has a power-law relation between flux and frequency, i.e. for i -th source, $S_f \propto f^{-\alpha_i}$. To convert Gaia units of $e^{-\text{s}^{-1}}$ into Jy, we multiply S_f with a corrective factor c_f . This means the observed flux density is $S'_f = c_f S_f$. For calculating α_i , we use the color magnitude m_{G-BP} . As Gaia and subsequently Quaia magnitudes are given in Vega system, we use the mean wavelength and zero points (ZP) of the G and BP bands [Riello 21] and write

$$m_f = -2.5 \log_{10} S'_f + 2.5 \log_{10} c_f + \text{ZP}. \quad (3.1)$$

and hence

$$m_{G-BP} = 2.5 \log_{10} (S'_{BP}/S'_G) + 2.5 \log_{10} (c_G/c_{BP}) + k \quad (3.2)$$

$$\implies \alpha_i = \frac{\varepsilon + k - m_{G-BP}}{2.5 \log_{10} (f_{BP}/f_G)} \quad (3.3)$$

with $k = ZP_G - ZP_{BP}$, ε is $2.5 \log_{10} (c_G/c_{BP})$, and we have used $S'_f = c_f S_f$ in the final step. The equation 3.3 gives a distribution of spectral index, as shown in left plot of Fig. 3.4. The mean values have been shown for illustrative purpose and do not hold any special significance in our calculations.

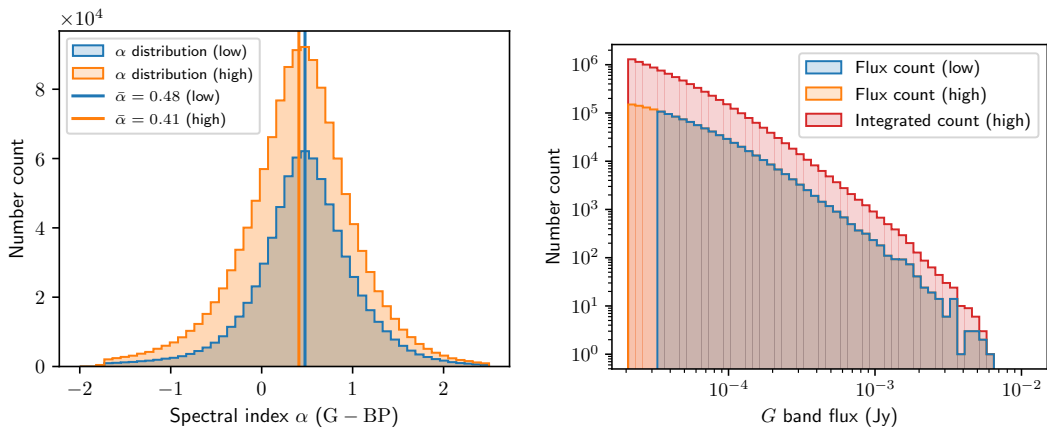


Figure 3.4: (a) Distribution of spectral indices in the Quaia low and Quaia high. Orange and Blue denote Quaia high and Quaia low respectively. The mean spectral indices are indicated by the vertical lines, (b) Source number counts binned by G band flux. Red histogram shows the integrated source count above a limiting flux density.

Source number counts

For calculating flux distribution, we convert the G band magnitude into the Gaia system (in units of photoelectrons per second) by using the ZPs mentioned above. These are then converted into Jy units by applying the conversion factor c_v from Gaia documentation [European Space Agency 21]. This distribution along with the integrated distribution (number of sources above some limiting flux density) are shown in right plot of Fig. 3.4.

Dipole amplitude calculation

Since our source count distribution in Fig. 3.4 is not a straight line, we need to use the modified dipole amplitude expectation method discussed in Introduction. For Quaia low, since $G = 20.0$ corresponds to $S \approx 3.27 \times 10^{-5}$ Jy, we use $S_0 = 3.3 \times 10^{-5}$ Jy, while for Quaia high, $G = 20.5$ corresponds to $S \approx 2.06 \times 10^{-5}$ Jy, so we use $S_0 = 2.1 \times 10^{-5}$ Jy.

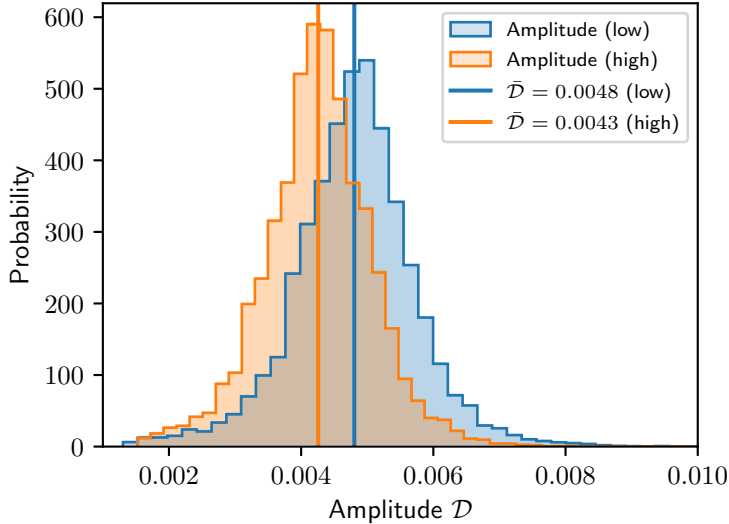


Figure 3.5: Probability distribution for the dipole amplitude assuming v_{CMB} .

Then substituting $v = v_{CMB}$, sampling 25000 random spectral indices from Fig. 3.4, and performing the analysis, we get the distributions shown in Fig. 3.5. The mean values for $\bar{\mathcal{D}}$ are $\bar{\mathcal{D}} \approx 0.0048$ for Quaia low and $\bar{\mathcal{D}} \approx 0.0043$ for Quaia high.

3.3.3 Choice of priors

Finally, we need to determine the priors $\pi(\Theta|M)$ on free parameters of each model, which will be used along with the likelihood functions to determine the posterior distribution for the parameters. The choice of priors is reflective of our belief about the parameter's values without relying on the data.

1. For mean number densities (monopole) \bar{N} , we adopt $\bar{N} \sim \mathcal{U}[0, 50]$ for Quaia high and $\bar{N} \sim \mathcal{U}[0, 30]$ for Quaia low.
2. For dipole amplitude D and double dipole amplitudes D_1, D_2 , we utilize a uniform distribution $D, D_1, D_2 \sim \mathcal{U}[0, 1]$. This choice is motivated by the significant uncertainty in dipole magnitude for a range of statistically independent tests (for some examples, refer to [Kumar Aluri 23]). The quadrupole amplitude is sampled from $\tilde{D} \sim \mathcal{U}[-1, 0]$, since a positive prior restricts it to a bad fit at the north galactic pole.
3. For directions, we use equatorial coordinates (RA, co-dec) in radians and denote them by (θ, ϕ) . For dipole direction, we used $\phi \sim \mathcal{U}[0, 2\pi]$ and $\theta \sim \cos^{-1}(1 - 2u)$ where $u \sim \mathcal{U}[0, 1]$. For double dipole, we used $\theta_1, \theta_2 \sim \cos^{-1}(1 - 2u)$ and $\phi_1, \phi_2 \sim [3\pi/2, 5\pi/2], [\pi/2, 3\pi/2]$, essentially scanning different hemispheres to avoid cross-talk between the directions. In a similar spirit, we used $\phi \sim [\pi/2, 3\pi/2]$ and $\theta \sim \cos^{-1}(1 - 2u)$ for the quadrupole model.

3.4 Results

3.4.1 Quaia Low

Low galactic masks: $|b| < 10^\circ, 20^\circ, \text{ and } 30^\circ$

This masking regime is dominated by the double dipole model (M_2), as is seen from the Bayes factors in tables A.1 and A.2. It is important to note that the level of support is same for both point-by-point and Poisson likelihoods.

In order to understand the results better, consider the list of Bayes factors for a 30° mask for point-by-point likelihood i.e. column 4 of Table A.1. Here, double dipole (M_2) is the preferred hypothesis with a strong level of support as compared to the dipole (M_1), with $\ln B_{21} = 4.5$. Kinematic dipole (M_6) has the second highest Bayes factor, and yields a relative Bayes factor of $\ln B_{25} = 3.4$, with respect to M_2 . In fact, M_6 has the lowest relative Bayes factor as compared to M_2 for the $|b| < 30^\circ$ galactic mask. However, as we move towards less conservative galactic masks ($|b| < 10^\circ, 20^\circ$), M_1 starts catching up to M_2 . In the same domain, kinematic velocity model (M_5) is has the third highest Bayes factor followed by M_6 .

High galactic masks: $|b| < 30^*, \text{ and } 40^\circ$

For a $|b| < 40^\circ$ mask, kinematic dipole (M_6), where the dipole is completely aligned with the CMB dipole and has a CMB velocity dependent amplitude, has the highest Bayes factor, while kinematic direction (M_4) and kinematic velocity (M_5) have the second and third highest Bayes factors. Again, like the Low galactic mask regime, the dominance is consistent for both point-by-point and Poisson likelihoods.

This highlights the transition happening from $|b| < 30^\circ$ to $|b| < 40^\circ$ galactic masks, where the support for kinematic hypotheses $M_4 - M_6$ increases substantially as compared to the fitting hypotheses $M_1 - M_3$. This transition is also seen for the 30^* mask which is a superposition of $|b| < 30^\circ$ mask with a 4 sr circular mask centered at the origin of galactic coordinates. There, both M_2 and M_6 have comparable Bayes factors, which implies that 30^* mask is an intermediate stage for this transition.

3.4.2 Quaia high

Low galactic masks: $|b| < 10^\circ, 20^\circ, \text{ and } 30^\circ$

Here again like Quaia low, double dipole (M_2) is the prevailing model, as evident from equal level of support in Tables A.3 and A.4 for point-by-point and Poisson likelihoods.

Consider again, the list of Bayes factors for a 30° mask for point-by-point likelihood i.e. column 4 of Table A.3. Unlike Quaia low, both M_2 and M_1 have equal support i.e. $\ln B_{21} = 0$, while for Poisson likelihood, Bayes factor for M_2 is slightly higher than M_1 . This slight shift in Bayes factor does not impact the interpretation significantly, as it is representative of a marginal support for M_2 over M_1 . Curiously, the kinematic velocity model (M_5), which has the third highest support has a relative Bayes factor of $\ln B_{25} = 14.3$, indicating overwhelming support for M_2 and M_1 for a 30° mask.

In case of less conservative masks, M_2 is overwhelmingly favoured over other models, and M_1 in particular, with the level of support increasing with a decrease in mask angle.

High galactic masks: $|b| < 30^*$, and 40°

For a 40° mask, the kinematic direction hypothesis (M_4) is the preferred hypothesis. However, Bayes factors for all hypotheses (with respect to M_0), except M_3 are comparable, with maximum Bayes factor difference being ≈ 1 in log units between M_4 and M_1 . This is suggestive of each model have equal explanatory power, and hence being on similar footing.

For a 30^* mask, M_1 is the favoured hypothesis, followed by M_6 . The level of support for M_1 is in general higher than the support for M_4 in a 40° mask, indicating dipole's dominance in this regime.

3.5 Discussion

3.5.1 Dominance of Double Dipole

Let's first discuss about the dominance of double dipole at low galactic masks in both Quaia high and Quaia low, as outlined in 3.4.1 and 3.4.2. What we need to understand is why a model with more parameters, despite being penalized by the Occam factor for its complexity, can explain the data in a better way as compared to other models.

To understand this, we extracted the mean values of the posterior distribution of the double dipole with a 30° mask, and computed the signal term $f_i = (1 + \mathbf{D}_1 \cdot \hat{\mathbf{p}}_i) \times (1 + \mathbf{D}_2 \cdot \hat{\mathbf{p}}_i)$ for each pixel in the sky and the resultant map is shown in Fig. 3.6. Clearly, the high Bayes factor is due to the over-density at $(l, b) \approx (0^\circ, 30^\circ)$ and under-densities along the galactic plane from $l = 120^\circ$ to $l = 240^\circ$. These features are not adequately captured by the dipole M_1 and are asymmetric, so quadrupole M_3 is not a good fit for the data. Instead, the double dipole M_2 , captures these features for both Quaia high and Quaia low for low galactic masks, since these features are mostly within $|b| < 30^\circ$. This claim is further strengthened by the results for 30^* mask, which effectively mask out the remaining over-density region above $b = 30^\circ$, and hence showcasing, low support for the double dipole.

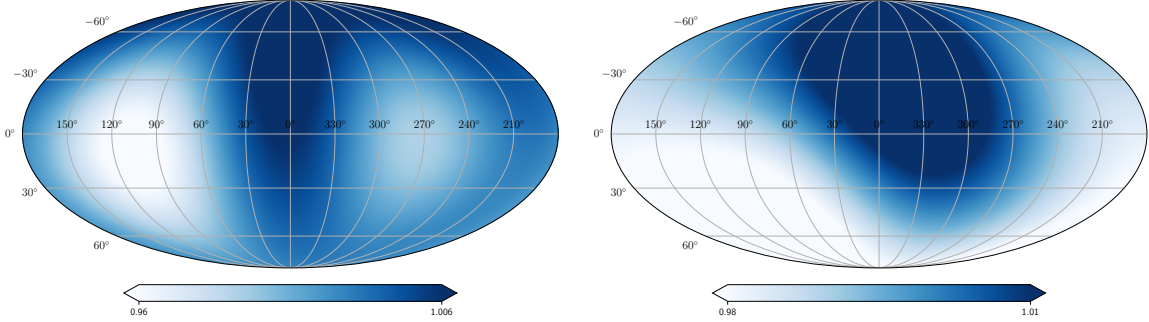


Figure 3.6: Reconstructed signal using the best fit parameters for double dipole tested on a 30° mask. The nature of this signal is similar to the pattern of over-densities and under-densities seen in Quaia catalogue. (a) Left panel is for Quaia low ($G < 20.0$), (b) right panel is for Quaia high ($G < 20.5$).

Because of this, we believe that systematic effects due to Quaia selection function affects our analysis. These effects, arising due to over estimation of dust, stellar contamination, etc. contribute to overdensity region above the galactic plane, hence giving incorrect fits in probing the quasar distribution.

To understand the effect of over-density, it is imperative to examine the shift in dipole amplitude and direction for M_1 model with an increase in galactic mask angle. This is shown in Fig. 3.7 for both Quaia low and Quaia high. An inspection of Quaia low (top panel) reveals that as over-density region near the Galactic center is masked out by an increasing galactic plane mask, the dipole direction shifts towards the kinematic dipole. For a 40° mask, the direction is consistent with CMB within $\approx 0.5\sigma$. It is important to note that at this stage, more than half of the sky has been masked and hence the uncertainty in parameters has increased drastically. Inspecting the inferred dipole amplitudes (mentioned below the Quaia low panel in Fig. 3.7)- as over-dense region is progressively masked out, the inferred amplitude agrees with the kinematic value. In fact, for a 40° mask, the inferred amplitude $D \times 10^3 \approx 11_{-5}^{+6}$ is consistent with the kinematic expectation of $D \times 10^3 \approx 8$, which explains why M_6 is preferred in this regime.

This signifies that spurious over-densities are removed by a 40° galactic mask and the remaining data gives a dipole consistent with the kinematic dipole. An attempt to remove this over-dense region was made by creating the 30^* mask. This mask covers some region beyond the $|b| = 40^\circ$ limit and hence removes the over-densities above galactic center. However, for this mask, the Bayes factors for M_6 and M_2 are comparable, implying that both have equal explanatory power. This can be caused by the presence of some other density fluctuations that are being masked out by the 40° mask but not by the 30^* mask. Therefore, a 40° mask is best suited for determination of cosmic dipole in Quaia low.

In case of Quaia high, a similar interpretation is not possible. A look at the bottom panel of Fig. 3.7 will reveal that the recovered dipole drifts away from CMB dipole in the

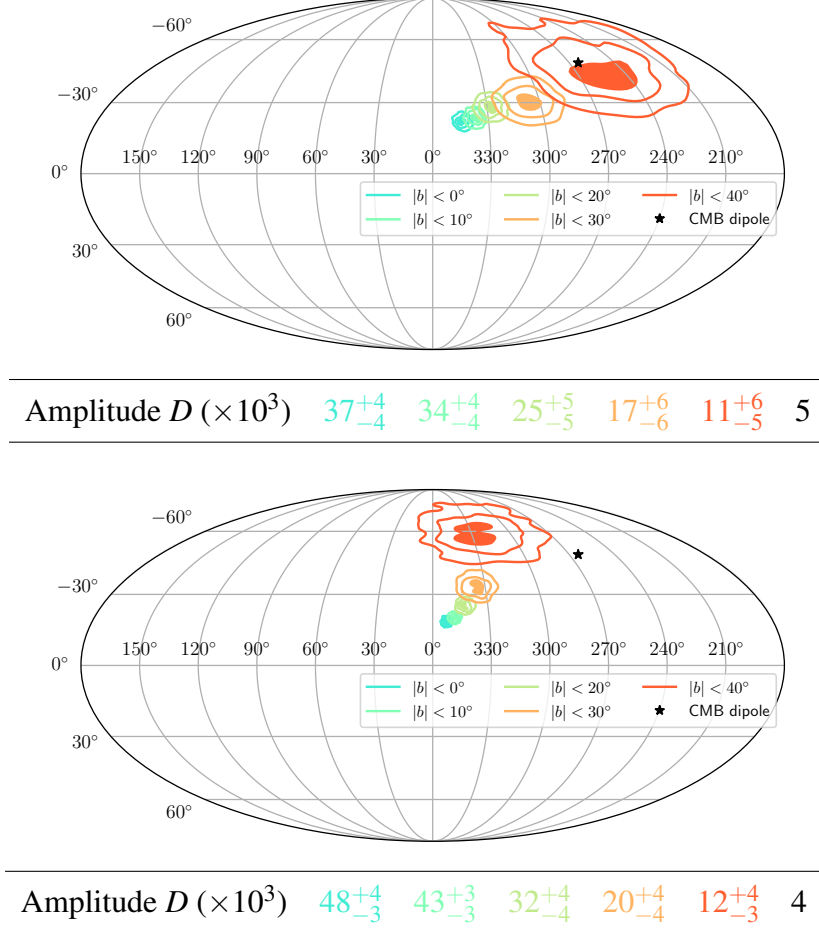


Figure 3.7: Projection of the posterior distribution for recovered dipole direction (in galactic coordinates). The contours give intervals of 0.5σ , 1σ and 1.5σ . As shown in legend, different colors correspond to different masks. Amplitudes of the recovered dipole ($\times 10^3$) are also tabulated beneath the plots with the same colour code as the sky projections. The listed uncertainties give a 2σ interval. (a) Quaia low on top, and (b) Quaia high in bottom.

direction of $(l, b) \approx (330^\circ, 60^\circ)$ as galactic mask size is increased. Furthermore, even with a 40° mask, the CMB dipole amplitude and inferred dipole amplitude do not agree within 2σ . Looking at the Bayes factors, for a 40° mask, M_4 is the favoured hypothesis, but the support is only marginal as the next hypothesis M_1 lags by $\ln B_{41} \approx 0.3$. So, we feel that although we can infer the presence of a dipole from Quaia high, yet we cannot constrain its parameters. The reason might be because, although there is an extra parameter in M_1 as compared to M_4 which gives it a favourable Occam factor, yet it has less explanatory power, which balances out the support for both models. Because of this, we are hesitant to draw any conclusion from Quaia high.

3.5.2 Contamination in Quaia high

Due to building evidence for contamination in Quaia high, a final check is in order. Accordingly, we test the following model on both Quaia low and Quaia high. Suppose that Quaia high is indeed contaminated, such that it consists of some dipole aligned with Quaia low (L) and a contamination (C). Then the dipole in Quaia high (H) would be a combination of L and C . Using Poisson statistics, the rate parameter for Quaia high would be (for i -th pixel)

$$(\lambda_i)_H = (\lambda_i)_L + (\lambda_i)_C \quad (3.4)$$

$$= \bar{N}_L (1 + \mathbf{D}_L \cdot \hat{\mathbf{p}}_i) + \bar{N}_C (1 + \mathbf{D}_C \cdot \hat{\mathbf{p}}_i) \quad (3.5)$$

The ‘C’ sample contains those quasars which are present in Quaia high, but not Quaia low. Note that we do not subtract Quaia low from Quaia high to construct the C , because of the nature of selection function. Instead C components are extra parameters in our model and are inferred during the fitting. The net likelihood is given by

$$\ln \mathcal{L}_{\text{tot.}} = \sum_{i=1}^{n_{\text{pix.}}} \ln P(N_i | \Theta_L) + \sum_{i=1}^{n_{\text{pix.}}} \ln P(N_i | \Theta_H). \quad (3.6)$$

and the parameter space is $\Theta_H = \{\Theta_L, \bar{N}_C, D_C, l_C, b_C\}$ and $\Theta_L = \{\bar{N}_L, D_L, l_L, b_L\}$, because $(\lambda_i)_H$ now depends on $(\lambda_i)_L$ as well.

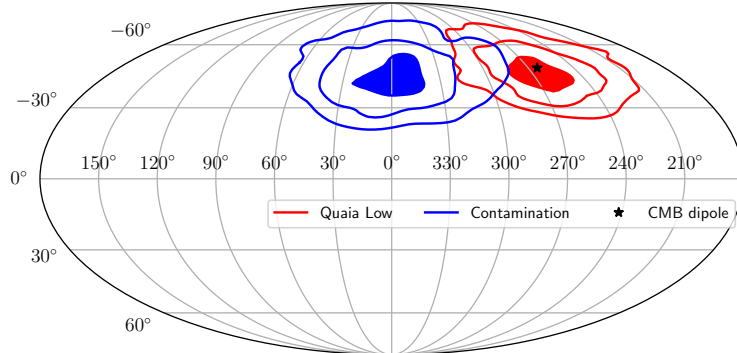


Figure 3.8: Projection of the 2D posterior distribution for the Quaia low dipole and the contaminated dipole, using a 40° mask. The contours give 0.5σ , 1σ and 1.5σ intervals.

We test this likelihood on a 40° mask for both Quaia high and Quaia low. The inferred dipole directions are shown in Fig 3.8. As expected, the Quaia low dipole is recovered nicely (compare with 3.7), and coincides with the CMB dipole. On the other hand, the contamination dipole, coincides with the over-density region near the galactic center. This supports our claim of Quaia high being contaminated by sources near the galactic center.

This means that while a 40° mask removes the over-density regions for Quaia low, it

is unable to do the same for Quaia high. So, we cannot rely on Quaia high to infer the cosmic dipole from quasars. Instead, we use Quaia low with a 40° mask to infer the cosmic dipole from this sample, because it removes the clustering issues arising due to the selection function. In case of Quaia high, the sample is contaminated by sources that are not part of quasar background, and the best we can say is that there is a dipole, without commenting on its parameters.

3.5.3 Dipole estimation for Quaia

Having completely understood our results, its time to present our main result: the cosmic dipole in Quaia. Based on the foregoing, we take the result for Quaia low 40° mask, and reserve our conclusions regarding Quaia high. For Quaia low, M_6 hypothesis: a dipole aligned with CMB dipole direction and having a kinematic amplitude, is the best explanation for the results. The model has positive support over other models such as the M_5 (dipole with CMB amplitude) and M_4 (dipole aligned with CMB direction). Hence, the dipole inferred from Quaia low quasars is consistent with the CMB dipole, and is thus consistent with CP.

3.6 Impact of priors on the results

During our discussions with Quaia authors, it was pointed out that since marginal likelihood (evidence) is an integral over the parameter space, it is sensitive to the choice of priors. Although it will not affect the posterior distribution for the parameters, yet it can affect the inferences drawn from Bayes factors for comparing competing hypotheses. Thus, we investigated the effect of narrower dipole amplitude priors on our findings. In particular, we reduced our priors by an order-of-magnitude and adopted $D \sim [0, 0.1]$ for dipole amplitude and $\tilde{D} \sim [-0.1, 0]$ for quadrupole amplitude.

We find that even though individual Bayes factors change, yet our conclusions are not affected. For Quaia Low the general trend was an increase in evidence values and hence Bayes factors for M_1 , M_3 and M_4 , but the relative support remained the same. For example, with a $|b| < 40^\circ$ mask on Quaia low, M_1 switched from $2.8 \rightarrow 5.2$, M_3 transitioned from $0.5 \rightarrow 2.9$, while M_4 shifted from $5.8 \rightarrow 8.0$ for both point-by-point and Poisson likelihoods. So, while the support for M_4 has increased, yet it only has slight preference over M_6 (with a Bayes factor of 7.3). For Quaia high, M_4 has marginally extra support than M_1 , but due to reasons mentioned in the foregoing, we reserve any conclusions. So, consistent matter and CMB dipoles are still favoured by restrictive priors.

Having determined the cosmic dipole in quasars, we now turn our attention to radio galaxies. This is the subject of next chapter.

Chapter 4

NVSS and RACS radio galaxies

4.1 Background

The number count dipole in radio galaxies was first studied in [Blake 02], where the authors reported broad agreement (within the computed uncertainties) of the NVSS radio galaxy dipole with the kinematic dipole. However, many subsequent studies have departed from this result and have reported a discrepancy between the radio galaxy inferred matter and the kinematic dipole. [Singal 11] reported that the NVSS dipole aligns with the kinematic dipole, but had four times larger amplitude. Subsequent works such as [Gibelyou 12, Rubart 13, Colin 17, Siewert 21, Wagenveld 23] reported similar trend by studying additional catalogues such as VLASS and RACS. These results have shaped the prevailing sentiment that the matter dipole aligns with the kinematic dipole, but has an excess amplitude [Kumar Aluri 23].

An additional point to understand is the effect of local structure on the matter dipole. Some studies like [Wagenveld 23] have assumed that since most of the sources are at high redshift, so the contribution of local sources to the matter dipole would be negligible. Others (such as [Tiwari 16, Dam 23, Cheng 23]) have studied the effect of local structure on the matter dipole using a variety of theory motivated arguments to construct a ‘clustering dipole’ term. Since the matter dipole has consistently been reported to have an excess amplitude, it is worthwhile to study the effect of local structure on the radio galaxy dipole.

Hence, this chapter is dedicated to studying matter dipole in radio galaxy distribution. We revisit two catalogues which have contributed to the dipole anisotropy tension: NVSS [Condon 98] and RACS-low [Hale 21]. We utilise Bayesian statistics to study the matter dipole and the effect of local structure on its amplitude and direction. *The work presented here has been submitted to MNRAS and is currently under review.*

4.2 Catalogue Preparation

4.2.1 RACS

The Rapid ASKAP Continuum Survey-low (RACS-low) [Hale 21] was conducted with the ASKAP facility in southern hemisphere at a central frequency of 887.5 MHz between 2019 and 2022, covering the sky with $\delta \leq 41^\circ$. As the survey resolution changes with declination, an extra catalogue was constructed from data convolved to 25 arcseconds resolution. This version was utilised for this work and, we refer to it as RACS for the rest of this thesis. But, some observational tiles could not be convolved to the common resolution, hence the effective coverage for the catalogue used by us is $-80^\circ \leq \delta \leq 30^\circ$. In addition, the galactic plane was excluded by imposing $|b| < 5^\circ$. This leaves us with a catalogue of about 2.1 million sources with a 67.9% of sky coverage.

To prepare the catalogue for analysis, we need to impose appropriate flux cuts to mitigate completeness issues. We will work with peak flux density for RACS. Although RACS is 95% complete at 3 mJy, we find improvements in sample's homogeneity with a 10 mJy flux cut. To support our point, we plot variations in source density as a function of declination for different flux limits in left plot of Fig 4.1. As we move from 2.5 mJy cut to 10 mJy cut, the average percentage deviation from mean density decreases from 1.6% to 0.9%, while it again increases to 1.0% for a 15 mJy flux cut. Accordingly, we choose a 10 mJy flux cut for our analysis. The corresponding flux distribution is shown in right plot of Fig 4.1.

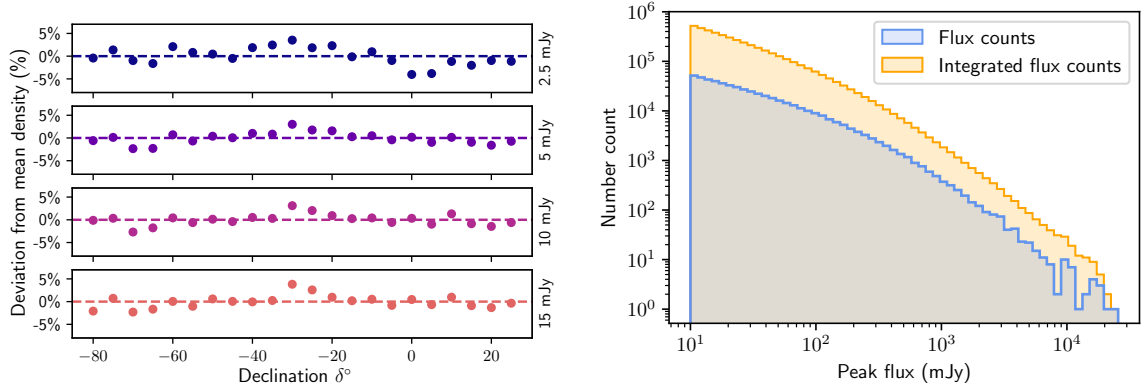


Figure 4.1: *Left:* Deviation from NVSS mean source density (%) by declination angle for different flux cuts. *Right:* Flux distribution of the RACS(B) sample, shown in blue, in which a 10 mJy flux limit has been used. The total number of sources above a limiting flux density are shown in yellow.

Next, we need to mask the density fluctuations. First, we remove under-dense pixels along the edge of galactic plane. Next, we mask the excluded survey tiles at southern equa-

atorial pole using a disc of radius 13° . This is followed by masking an additional degree of declination in northern equatorial hemisphere. Thus, our final sample covers a declination range of $-77^\circ \leq \delta \leq 29^\circ$. Finally, we mask four regions with low source counts, corresponding to under-dense tiles in RACS merged sky catalogue. Their positions, radius and nearby bright radio sources are specified in Table B.1. We mask these regions with discs of radius 3° . This leaves us with a sample of 524651 RACS sources as shown in left plot of Fig 4.2. We refer to this sample as RACS(A) variant.

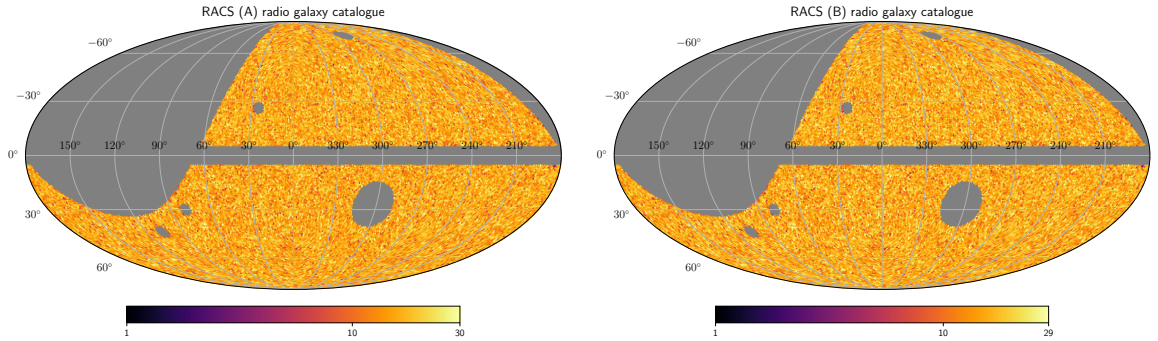


Figure 4.2: *Left:* Processed RACS catalogue with local sources included i.e. RACS(A). *Right:* Processed RACS catalogue with local sources excluded i.e. RACS(B). Color bar indicates the number of sources per HEALPixel

Local clustering

We investigate the effect of clustering by creating an additional variant of RACS. We cross-match RACS with local radio sources and remove them from the catalogue. Similar to [Cheng 23], we use the Two Micron All Sky Redshift Survey 2MRS [Huchra 12] and radio sources with $z \leq 0.01$ from NASA/IPAC Extragalactic Database (NED)¹. We find all RACS sources within 5 arcseconds of each local source and remove the nearest source. This is done after applying a flux cut, but before masking the sample. The cross-matching radius was selected because a typical RACS source position is accurate to 1 or 2 arcseconds. This identifies 3819 local objects in RACS, which are removed, leaving a final source count of 520885 after masking. We refer to this sample as RACS(B) variant, which is shown in right plot of Fig 4.2. Table C.1 gives a summary of the key choices made in processing the RACS.

4.2.2 NVSS

The NRAO VLA Sky Survey (NVSS) [Condon 98] was conducted using Very Large Array (VLA) in northern hemisphere at 1.4GHz, between 1993 and 1997, covering the sky with

¹<https://ned.ipac.caltech.edu/>

$\delta \geq -40^\circ$. The full source catalogue consists of 1.8 million sources. NVSS uses two configurations of VLA for different declination ranges: the D configuration for $-10^\circ \leq \delta \leq 78^\circ$, while DnC for remaining portion of the sky. This means that although NVSS claims to reach 100% completeness by 4mJy, it would still show a strong systematic bias in number density. We mitigate this by using a sufficiently bright flux cut.

We will work with integrated flux density for NVSS and plot of source density variations with declination for different flux limits (left plot of Fig 4.3). As we move from 2.5 mJy cut to 15 mJy cut, the average percentage deviation from mean density decreases from 1.9% to 0.9%. Accordingly, we choose a 15 mJy flux cut for our analysis. This choice is in line with previous studies such as [Tiwari 16] and [Wagenveld 23]. The corresponding flux distribution is shown in right plot of Fig 4.3.

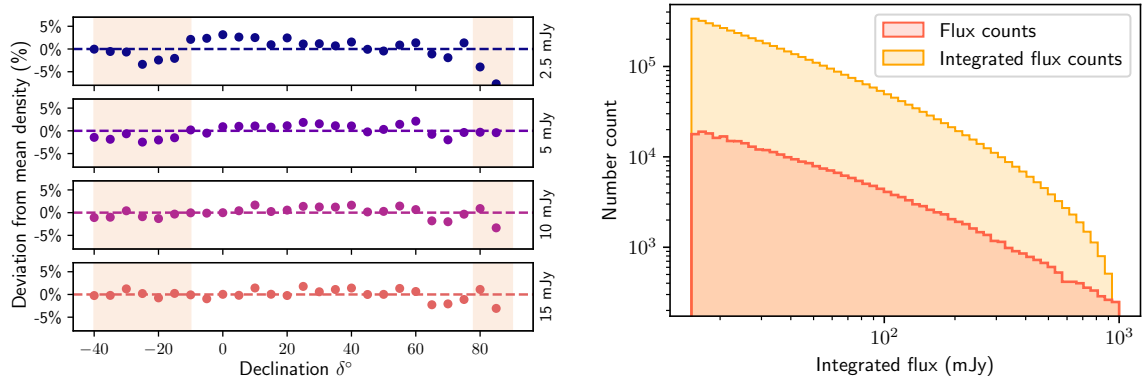


Figure 4.3: *Left:* Deviation from NVSS mean source density (%) by declination angle for different flux cuts. The declinations using the DnC configuration are shown in the shaded light brown region, and the D configuration region is left unshaded; *Right:* Flux distribution of the NVSS(B) sample, shown in red, in which a 15 mJy flux limit has been used. The total number of sources above a limiting flux density are shown in yellow.

For masking the density fluctuations, we remove the high source density regions around the galactic plane by a $|b| \leq 10^\circ$ mask. Next we remove regions with spuriously high source counts by following the masking choices of [Cheng 23]. Firstly, we mask all pixels surrounding sources with flux greater than 1Jy because, bright and extended sources can appear as multiple entries in the catalogue. Secondly, we visually identify four regions with high source counts and mask these regions with a disc of radius 3° . The position, radius and nearby bright radio sources are specified in Table B.2. Finally, to remove low source count pixels near the survey limit, we mask an additional degree north of $\delta = -40^\circ$. This leaves us with a final source count of 342308 as shown in left plot of Fig 4.4. We refer to this sample as NVSS(A) variant.

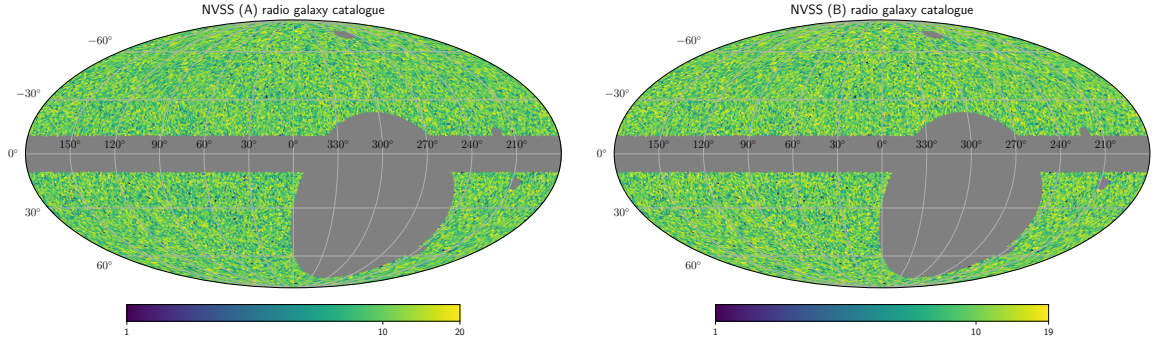


Figure 4.4: *Left:* Processed NVSS catalogue with local sources included i.e. NVSS(A). *Right:* Processed NVSS catalogue with local sources excluded i.e. NVSS(B). Color bar indicates the number of sources per HEALPixel

Local clustering

We repeat the cross-matching procedure for RACS. NVSS has a positional accuracy of 1 arcsecond after 15 mJy flux cut. Therefore, we again use 5 arcseconds as the cross-matching radius. We identify 3083 common sources, which we remove, and we are left with 339425 sources after masking. We refer to this sample as NVSS(B) variant, which is shown in right plot of Fig 4.4. Table C.2 gives a summary of the key choices made in processing the NVSS.

4.3 Processing pipeline

4.3.1 Dipole amplitude expectation

Spectral index

Unlike the Quaia quasars, both RACS and NVSS list flux densities at a single frequency, hence we do not get information about a source’s spectral index in a straight-forward way. Typically, the spectral index for a synchrotron assumed emission mechanism is used i.e. $\alpha \approx 0.75$ (see for example [Secrest 22]). Often, overlapping sources between different radio surveys at different frequencies are used to determine the spectral index distribution, which usually has a median of $\alpha \approx 0.75$. A notable example is [Mauch 03], where Fig 8 gives the spectral index distribution of NVSS sources that overlap with Sydney University Molonglo Sky survey (SUMSS), and shows a broad distribution with median $\alpha \approx 0.83$. Although the kinematic dipole amplitude is not very sensitive to the exact value of α , yet we assume that the median α is 0.75. Since the largest dispersion in Fig 8 of [Mauch 03] is 0.5, we assume a similar spread for NVSS spectral index. Accordingly, we describe our spectral index distribution by a Gaussian $\mathcal{G}(\mu = 0.75, \sigma = 0.5)$. For RACS, [Hale 21] found

α distributions by comparing the common sources with four surveys (including NVSS) at different frequencies. Their $\alpha \in [0.6, 0.9]$, with dispersion of the order ≈ 0.5 , hence we define spectral index distribution by the same Gaussian $\mathcal{G}(\mu = 0.75, \sigma = 0.5)$.

Dipole amplitude expectation

To calculate the expected dipole amplitude, we utilize the modified approach discussed in Chapter 1 with two additional steps

1. For the i -th source, we sample the spectral index α_i from the Gaussian $\mathcal{G}(\mu = 0.75, \sigma = 0.5)$.
2. For the i -th source, with flux S_i , we sample a new flux value S_i^* from a Gaussian $\mathcal{G}(\mu = S_i, \sigma = \Delta S_i)$ for flux measurement uncertainty ΔS_i .
3. After using $v = v_{\text{CMB}}$ and, sampling 10000 random catalogues, we calculate the mean of the expected amplitude in each case.

For RACS, we use $S_0 = 12$ mJy, and find the mean amplitude as $\mathcal{D}_{\text{RACS}} = (4.22 \pm 0.06) \times 10^{-3}$. For NVSS, we use $S_0 = 17$ mJy and find $\mathcal{D}_{\text{NVSS}} = (4.28 \pm 0.08) \times 10^{-3}$. This amplitude is calculated using B variant for each catalogue (expected amplitude for A variant is same as B variant)

4.3.2 Likelihood function and choice of priors

We choose to work with point-by-point likelihood since its computationally less expensive and gives the same results as Poisson likelihoods. Next we need to define a method for joint analysis of the two radio catalogues. Previous research works such as [Darling 22] and [Colin 17] combined multiple radio galaxy catalogues by scaling the fluxes according to source spectral index, removing the common sources and then creating a single catalogue. As shown in [Wagenveld 23], this ignores varying systematic effects and hence gives a spurious dipole signal. Hence, we use a different approach. Since both catalogues will have a similar dipolar modulation (note that different flux and spectral index distribution implies different dipole amplitudes), we fit the dipole to each catalogue separately, but combine the information across catalogues with joint likelihood function given by

$$\ln \mathcal{L} = \ln \mathcal{L}_{\text{NVSS}} + \ln \mathcal{L}_{\text{RACS}} \quad (4.1)$$

where the individual likelihoods are given by 2.12. The parameter space for this likelihood is $\Theta = \{\mathcal{D}_{\text{NVSS}}, \mathcal{D}_{\text{RACS}}, l, b\}$. The priors for different parameters were chosen as follows

- Similar to the case of quasars, we choose unconstrained priors on dipole directions i.e. $\text{RA} \sim \mathcal{U}[0, 2\pi]$ and $\text{co-dec} \sim \cos^{-1}(1 - 2u)$ where $u \sim \mathcal{U}[0, 1]$. We perform our calculations in equatorial coordinates and present our results in galactic coordinates.
- Dipole amplitudes are sampled uniformly from $\mathcal{U}[0, 0.1]$. This choice is reflective of a broad range of results from previous studies as showcased in [Kumar Aluri 23]

4.4 Results

4.4.1 RACS

The Bayes factors for different hypotheses for both RACS(A) and RACS(B) are shown in Table D.1. The corresponding inferred dipole parameters for dipole model (M_1) are shown in right corner-plots of Fig 4.5 (blue color scheme). Interestingly, the kinematic dipole model M_4 has the highest Bayes factors- and hence greatest explanatory power for both RACS(A) and RACS(B). A look at the corresponding corner plot for free dipole fit will show that the amplitude has decreased by ≈ 0.001 between RACS(A) and RACS(B), although the uncertainties still remain large.

4.4.2 NVSS

The Bayes factors are given in Table D.2, while the dipole fits for M_1 are shown in left corner-plots (red color scheme) of Fig 4.5. For NVSS(A), the kinematic direction model (M_3) has the highest bayes factor. This model assumes that the matter dipole aligns with the kinematic dipole, but the amplitude has no constraints. For this model, the inferred dipole amplitude is (with 2σ uncertainties) $\mathcal{D} = (12 \pm 5) \times 10^{-3}$. It is important to note that since M_1 and M_3 are different hypotheses, the inferred dipole amplitude need not match with each other.

In case of NVSS(B), it is observed that kinematic dipole (M_4) explains the data, albeit with ‘bare support’ since the next best explanatory model- M_3 has almost equal explanatory power with $\ln B_{43} = 0.4$. The free dipole amplitude again decreases by ≈ 0.002 between RACS(A) and RACS(B).

4.4.3 Joint analysis: NVSS+RACS

The Bayes factors are given in Table: D.3. Here, the kinematic dipole model (M_4) is the preferred hypothesis, with a ‘somewhat strong’ support as the next preferred hypothesis M_3 , lags by $\ln B_{43} = 2.9$. The corner-plot of inferred dipole parameters $\mathcal{D}_{\text{NVSS}}, \mathcal{D}_{\text{RACS}}, l, b$ for M_1 is shown in Fig. 4.6, while Fig. 4.7 shows the corresponding sky projection.

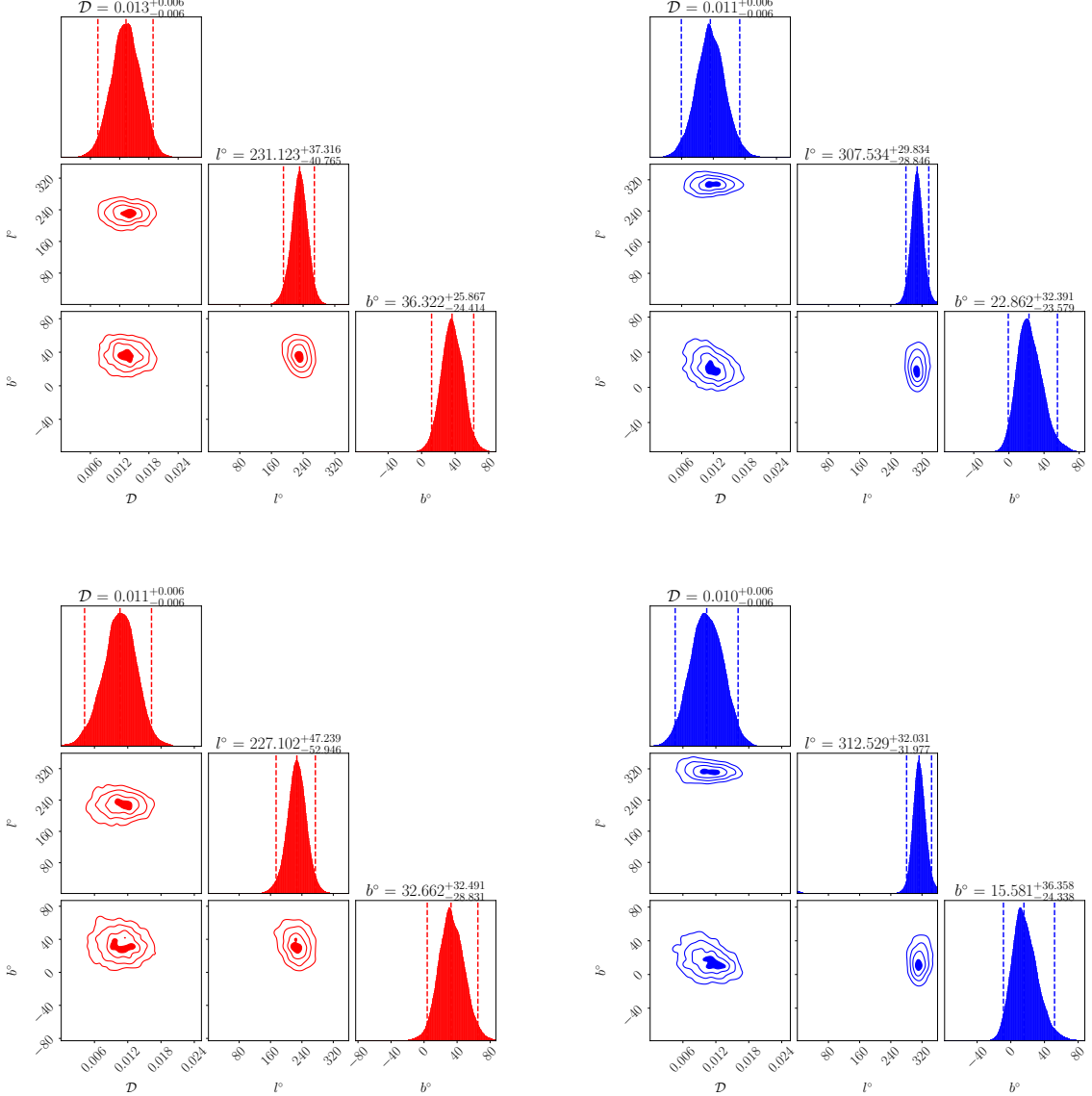


Figure 4.5: Corner plots for the free dipole model tested on our individual samples. The dashed lines on the histograms represent a 2σ interval on either side of the median. Quoted uncertainties above each 1D posterior also give 2σ confidence limits on each model parameter. The contours on the 2D marginal posteriors give intervals of 0.5σ , 1σ , 1.5σ and 2σ . *Left column (red)*: NVSS(A) and NVSS(B) samples. *Right column (blue)*: RACS(A) and RACS(B) samples.

4.5 Discussion

4.5.1 Effect of local clustering

The above mentioned results show that the matter dipole in both NVSS and RACS is consistent with the kinematic dipole. This is more evident when all the local sources are removed before analysis for both individual and joint analysis. As we move from A to B variants and remove the local sources, the inferred dipole amplitude diminished for both catalogues.

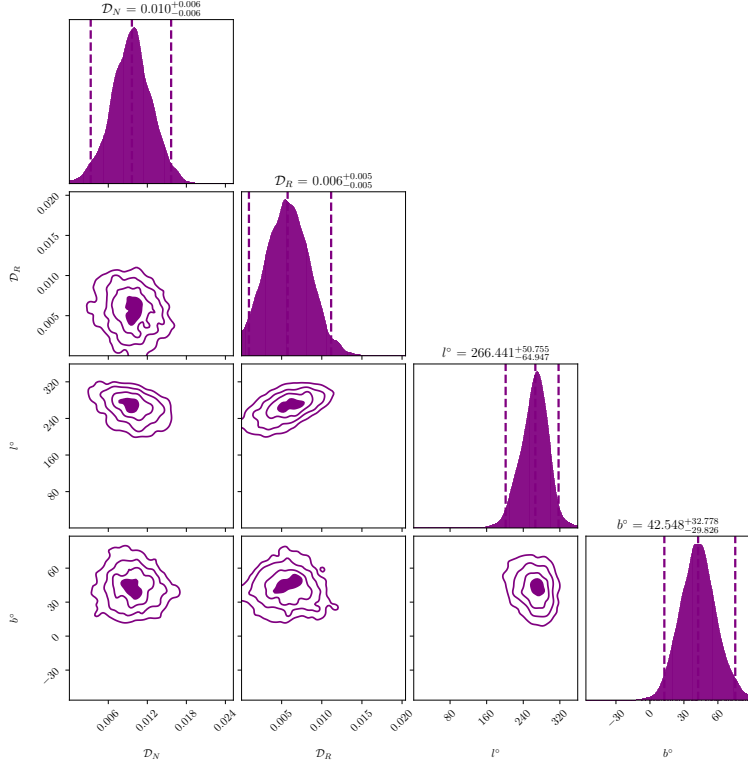


Figure 4.6: Corner plot for the joint RACS(B) and NVSS(B) analysis. The dashed lines on the histograms represent a 2σ interval on either side of the median. Quoted uncertainties above each 1D posterior also give 2σ confidence limits on each model parameter. The contours on the 2D marginal posteriors give intervals of 0.5σ , 1σ , 1.5σ and 2σ . \mathcal{D}_R refers to the RACS dipole amplitude ($\mathcal{D}_{\text{RACS}}$) and \mathcal{D}_N refers to the NVSS dipole amplitude ($\mathcal{D}_{\text{NVSS}}$).

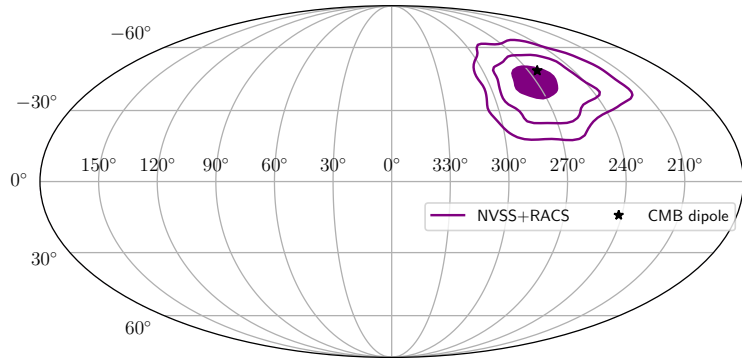


Figure 4.7: Projection of the posterior distribution for recovered dipole direction in joint analysis of RACS(B) and NVSS(B). The contours give intervals of 0.5σ , 1σ and 1.5σ .

We thus deduce that local sources impact the matter dipole amplitude. To put this in numbers, although about 3000 sources (0.9% of final source count) are removed from NVSS and about 4000 sources (0.7%) are removed from RACS, the dipole amplitude reduces by $\approx 20\%$ in both cases. This explains the high support for M_4 in the Tables D.2 and D.1.

Redshift evolution of clustering

To further probe the effect of local clustering on matter dipole amplitude, we probe the change in amplitude as a function of redshift. The 2MRS catalogue contains objects till a redshift of $z \approx 1$, while NED contains objects till $z \approx 0.01$. Although the homogeneity scale for the universe is smaller than $z \approx 0.1$, the exact number is still a matter of debate (see [Kumar Aluri 23] for details). Although there are some works like [Scrimgeour 12] that place this transition at $z \approx 0.023 - 0.027$ or $110 - 115 Mpc$ assuming $h = 0.7$, these numbers have their own set of assumptions. So, we probe how deeper redshift cuts impact the clustering bias in the inferred dipole amplitude by fitting our models to different redshift bins. We systematically remove the sources within redshift bins of the form $z \in [0, n]$, where $n = 0, 0.01, 0.02 \dots 0.1$. The results are presented in Fig 4.8.

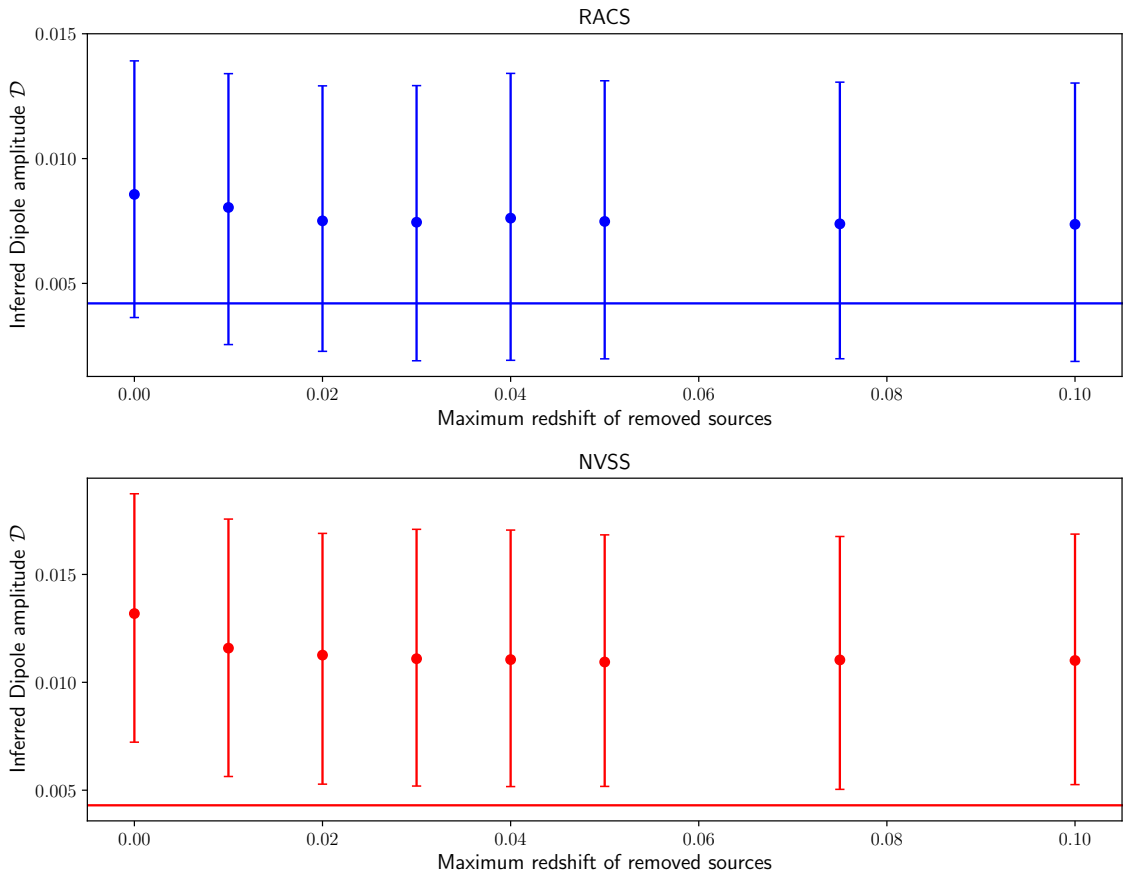


Figure 4.8: Inferred dipole amplitude against maximum redshift removed during cross-matching. The error bars represent a 2σ confidence limit. Blue is RACS and red is NVSS. The solid line indicates the expected dipole amplitude in each case.

In case of RACS, the inferred dipole amplitude and kinematic expectation agree with each other within 2σ for all redshift cuts. The agreement between both increases with an increase in the redshift bin size. For NVSS, we see that the inferred dipole amplitude decreases up to $z \approx 0.04$ and then becomes constant. This represents a co-moving length

scale of $\approx 170 Mpc$, which is somewhat more than the previous studies mentioned above. Although the 2σ errors in amplitude are quite significant, yet by $z \leq 0.03$ cut, the kinematic amplitude is just outside the 2σ error-bar.

The above paragraph warrants a study of the local structure being captured in the posterior distribution. We plot the spatial distribution of local sources from NED and 2MRS with a redshift $z \leq 0.02$ in the top panel of Fig 4.9. There, a significant band of local sources concentrated near the kinematic dipole direction is observed. As shown in middle and bottom panel of Fig 4.9, this band of structure is being picked up by the cross-matched sources of RACS and NVSS. It explains the decrease in inferred dipole amplitude till $z \leq 0.04$ as this local structure is being incrementally removed until the redshift bin covers its volume.

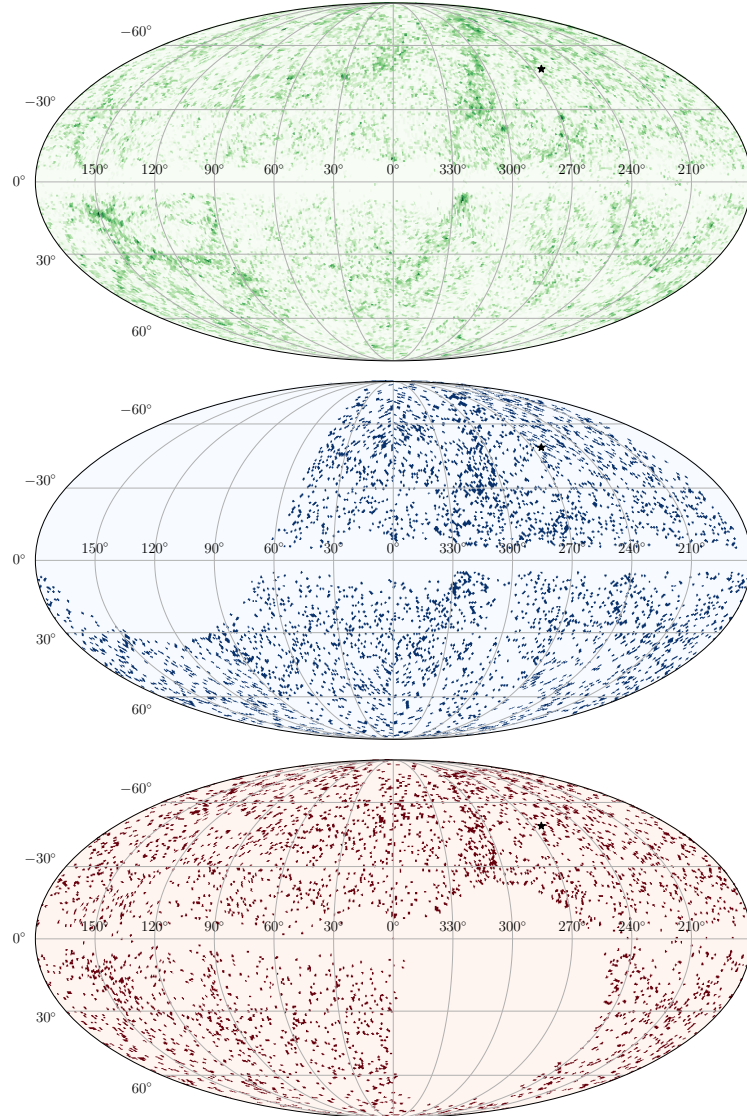


Figure 4.9: *Top:* NED and 2MRS sources with redshift less than 0.02. *Middle:* All 3819 cross-matched RACS-low(B). *Bottom:* All 3083 cross-matched NVSS sources removed in NVSS(B). The black star indicates the direction of the CMB dipole.

Effect of NED

Having identified the local structure affect our analysis, a discussion of NED’s impact on our study is in order. We aim to remove as many local sources as possible. However, NED collates sources from independent resources, hence the possibility of introduction of a bias due to completeness and coverage issues is not negligible. So, we performed our analysis without relying on NED, and only considering sources from 2MRS. Since, the cross-matched NED sources only represent $\approx 10\%$ of the total cross-matched sources, we find that our results are essentially unchanged with this modification. Therefore, our results are not affected by any unknown bias in NED sources and hence clustering has a genuine influence on the inferred matter dipole amplitude.

Clustering dipole

As a final check, we calculate the dipolar contribution of the local sources to the net matter dipole and, we dub this contribution as the ‘clustering dipole’. We take the cross-matched sources for RACS and NVSS and fit the free dipole model M_1 to them. The resulting posterior distribution for l and b is projected onto the sky as shown in Fig 4.10.

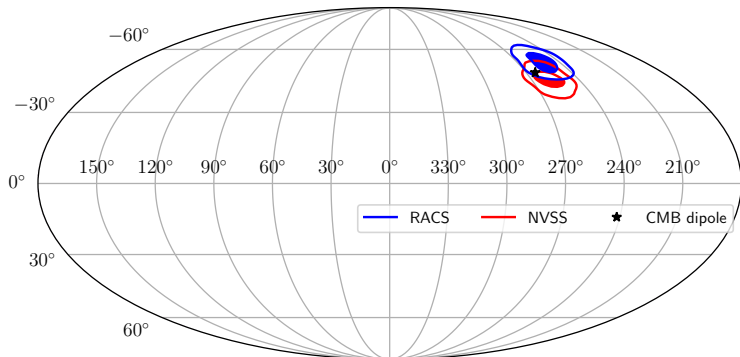


Figure 4.10: Projection of the posterior distribution for recovered dipole direction in the cross-matched sources. Blue indicates the RACS clustering dipole and red the NVSS clustering dipole. The contours give 0.5σ and 1σ intervals.

Surprisingly, the cross-matched sources show a well constrained dipole pointing near the kinematic dipole. Note that our priors assume that the clustering dipole might point towards any direction in the sky, as it traces the dipole in the local structures. Its even more curious that the dipole is not only well-defined with a small source count (< 4000), but also aligns with the CMB dipole direction. There are some studies like [Cheng 23], which postulate that the kinematic and clustering dipoles are correlated due to our local group’s motion towards a massive structure, but we feel that a further inquiry is needed into the nature of this local structure. Based on our analysis, we find that the clustering and matter dipoles act in synchronization to increase the inferred dipole amplitude. More specifically,

the clustering dipole contributes $\approx 10\%$ to RACS dipole amplitude and $\approx 15\%$ to NVSS dipole amplitude, which is determined from decrease in dipole amplitude as we move from variant A to B.

4.5.2 Joint analysis of RACS and NVSS

Following the above discussion, our joint analysis was performed using B variants i.e. after removing the local structure shown in Fig 4.9. Interestingly, the inferred dipole amplitudes for each catalogue in joint analysis decreased as compared to their values of individual analysis. Our inferred amplitudes are $\mathcal{D}_{\text{NVSS}} = (10 \pm 6) \times 10^{-3}$ and $\mathcal{D}_{\text{RACS}} = (6 \pm 5) \times 10^{-3}$ (see Fig 4.6). The kinematic amplitudes lie within the quoted uncertainties and, the kinematic dipole direction is within 5σ of the inferred dipole direction (see Fig 4.7).

At this point, we need to understand the reason behind a larger median dipole amplitude for NVSS as compared to RACS in both individual and joint analysis. Both NVSS and RACS had similar kinematic dipole amplitudes, suggesting minimal difference in the spectral index and flux distributions of either samples. The reason might be some further systematic effect biasing the inferred amplitude that has been adequately accounted for in RACS but not in NVSS. An example of such a biasing effect is that all local radio sources have not been removed in our cross-matching procedure. As seen in our analysis, the inferred dipole amplitude is sensitive to local clustering, which supports this point.

Previous studies have also reached at similar conclusion for NVSS. Using a fiducial model, [Cheng 23] estimate the clustering dipole to be $\approx (4 \pm 1) \times 10^{-3}$ with 80% of it arising due to objects below $z = 0.05$. Using mock NVSS catalogues, [Tiwari 16] estimate the clustering dipole contribution to be 70% of the total inferred dipole. Hence, while the top panel of Fig 4.9 represents the local structure quite well, it only sets a lower bound on the clustering dipole contribution as there might be additional unaccounted sources.

4.6 Comparison with other studies

The current literature on this problem agrees that the matter dipole and the kinematic dipole are pointing in the same direction, but the matter dipole has a larger amplitude as compared to the kinematic dipole [Peebles 22, Kumar Aluri 23]. So, are our results in tension with the previous analysis? Although our amplitude estimates have significant uncertainties and hence many of the previous findings are not precluded, yet it is important to look at some notable examples.

[Colin 17] accounted for local clustering in their analysis by cross-correlating with 2MRS. Still there was no significant impact on their matter dipole amplitude, which was

almost four times greater than the kinematic expectation. This lack of sensitivity to local sources is in direct conflict with our findings. However, the authors there combined NVSS with SUMSS to create NVSUMSS (roughly 600000 sources) by cutting the catalogues, scaling the flux densities and employing estimators, rather than performing a joint analysis with a likelihood function of the form of equation 4.1. A good follow-up would be to revisit their analysis from a Bayesian perspective and seeing if their contribution from SUMSS still gives a large dipole amplitude even after mitigating the clustering effects.

[[Secrest 22](#)] also examines the NVSS catalogue, and reports an amplitude of $\mathcal{D} \approx (12 \pm 3) \times 10^{-3}$, which is within 2σ uncertainties of our reported amplitude. However, the analysis does not account for the local sources, hence their median dipole amplitude is slightly higher than our inferred value. We reserve our comments on their joint analysis of NVSS and CatWISE2020 [[Marocco 21](#)] since the latter is a quasar catalogue. This means that our individual result for NVSS is compatible with both kinematic dipole and the dipole reported in [[Secrest 22](#)].

Finally, [[Wagenveld 23](#)] analysed RACS and NVSS jointly and reported an amplitude of $\mathcal{D} \approx (13 \pm 2) \times 10^{-3}$ (1σ errors), with a statistical significance of 4.8σ . The authors had a slightly different approach as compared to our analysis, since they assumed a common dipole for both RACS and NVSS, but their likelihood function was similar to ours. Although the 2σ uncertainties on NVSS amplitude in our joint analysis encompass their value, yet this is not the case for RACS amplitude. But the authors had assumed that clustering had negligible effect; contrary to our finding of a non-negligible effect. Most importantly, the authors report a tension with CMB dipole, contrary to our finding that CMB dipole is the most supported hypothesis. To resolve this discrepancy, we performed the joint analysis of both NVSS and RACS by assuming a single dipole in both models and fixed to the [[Wagenveld 23](#)] values of $\mathcal{D} = 13 \times 10^{-3}$, and dipole direction aligning with their median values. We report $\ln B = 3.9$ with respect to the null hypothesis, which when compared to Table D.3, still gives a strong support to the kinematic dipole. Hence, our conclusion differs from their findings.

Having analysed the cosmic dipole in radio galaxies, we have fulfilled the task that we intended to complete in this thesis. Hence, we conclude our major findings and discuss possible extensions to our work in the final chapter of this thesis.

Chapter 5

Summary and Concluding remarks

We have tested the assumption of isotropy by implementing the Ellis and Baldwin test on quasars and radio galaxies. We diverged from established convention of using frequentist statistics in this domain, and worked with Bayesian statistics. We conclude this thesis by summarising our major findings and commenting on some future work directions.

In Chapter 1, we investigated the impact of CP on modern cosmology, and methods to test it. We looked at the CMB thermal dipole, and how its kinematic interpretation led to the formulation of number count dipole test. We observed that for cosmological probes like quasars, the cumulative number counts are not a power-law function of the observed flux, and developed a modification to calculate dipole amplitude expectation for a kinematic interpretation. This method was implemented in subsequent chapters.

In Chapter 2, we studied Bayesian statistics and different levels of inference in Bayesian paradigm. This was followed by a study of nested sampling algorithm to calculate the ‘evidence’ integrals for a hypothesis. The algorithm worked by recasting the evidence integral from parameter space to likelihood space. Next, we motivated the choice of Poissonian and point-by-point likelihoods for our analysis, and modifying them to account for selection effects in case of quasars. Finally, we finished the chapter by a discussion on various hypotheses that were considered to infer the dipole from quasars and radio galaxies.

Chapter 3 was dedicated to determination of cosmic dipole from Quaia quasars. We find substantial evidence that the contamination in both Quaia low and Quaia high arise from the selection function. The reason might be over estimation of the effect of dust, which affects the inference of matter dipole from both the datasets. After masking the contaminated region, the matter dipole in Quaia low is consistent with the kinematic dipole, while the dipole parameters are not very well constrained for Quaia high. This is because Quaia high suffers from a large over-density just above the galactic center, something that was confirmed by contamination analysis. These results motivate the agreement of matter dipole and kinematic dipole in quasars.

Although our analysis is comprehensive, yet there are some interesting avenues which are open for exploration. Firstly, the Quaia selection function (as utilised by us) over-estimates the effect of dust and stellar contamination, and paves way for the presence of over-densities and under-densities around the galactic plane. Although these density fluctuations have been ignored in our analysis, but this has limited our ability to determine the cosmic dipole from Quaia, primarily by reducing the number of sources to roughly half of the total source count. This issue was discussed with Quaia authors, and they have released a new version of the selection function. Determination of cosmic dipole using the new selection function would be an interesting line of work. Secondly, our analysis has not taken the redshift distribution of quasars into account. A redshift binned selection function has been provided by the Quaia authors, but that is insufficient for calculations as there is a single redshift cut of $z = 1.47$. Future work might involve generating selection functions for various redshift bins and determining the evolution of cosmic dipole with their help.

Chapter 4 studied the cosmic dipole in NVSS and RACS radio galaxy samples. Our results questions the claimed tension between the matter and kinematic dipole. In light of our large uncertainties and small differences in Bayes factors, we are unable to decisively rule out the excess amplitude for individual analysis. Although our joint results agree with the CP, the effect of local structure needs further inquiry. We have shown that clustering effects are non-negligible for both RACS and NVSS. The contamination from local sources shifts the matter dipole amplitude to a larger value, which motivates the need for a detailed profiling of the local universe. Hence, we feel that the assumption of neglecting clustering effects is not valid, and in part accounts for the anomalously large matter dipole in radio galaxies. Curiously, clustering and kinematic dipole aligns nicely.

Some interesting extensions are as follows. Firstly, we are cross-matching near-infrared sources with radio sources. Generally, this is a non-trivial problem since radio sources are often extended with multiple (and often spatially distinct) components. In many cases it is unclear if the radio source indeed corresponds to the infrared source or not. Therefore, it is possible that during cross-matching procedure, we might have removed a single lobe of an extended radio structure. This point warrants further study in future. Secondly, the cross-matching radius was selected by considering positional accuracy of the RACS and NVSS sources. A better way of choosing this radius is to construct a ‘fake’ catalogue with random positional offset from the true catalogue, and evaluate the fraction of fake vs genuine cross-matches as a function of radius. This will give a better way of removing the effects of local structure. Finally, a joint analysis with other catalogues such as quasars, Sn-Ia etc. will give deep insights into this tension.

As a closing remark, we have studied the dipole anisotropy problem in detail, yet much remains to be done. But that is the topic of another thesis!

Appendix A

Table of Bayes Factors for Quaia quasars

Hypothesis	Galactic mask angle b°					
	0.0	10.0	20.0	30.0	40.0	30.0*
M_0 (Null)	0.0	0.0	0.0	0.0	0.0	0.0
M_1 (Dipole)	130.6	109.5	49.4	14.4	2.8	11.3
M_2 (Double Dipole)	175.0	130.6	57.7	18.9	0.2	14.5
M_3 (Quadrupole)	44.3	21.1	10.2	6.2	0.5	12.0
M_4 (Kinematic Direction)	23.4	30.5	24.0	12.8	5.8	13.2
M_5 (Kinematic Velocity)	30.4	27.8	17.7	9.1	5.3	7.5
M_6 (Kinematic Dipole)	16.2	18.4	15.7	11.0	7.3	10.1

Table A.1: Table of Bayes factors for different hypotheses and galactic masks for the Quaia low using the point-by-point analysis. The Bayes factors have been calculated with respect to the Null hypothesis M_0 . The 30^* mask is the combination of a 30° galactic mask and a 4sr circular mask centered at the $(l^\circ, b^\circ) = (0, 0)$. The highlighted cell represents the model with strongest support.

Hypothesis	Galactic mask angle b°					
	0.0	10.0	20.0	30.0	40.0	30.0*
M_0 (Null)	0.0	0.0	0.0	0.0	0.0	0.0
M_1 (Dipole)	131.4	109.9	49.9	14.5	3.5	11.7
M_2 (Double Dipole)	175.6	132.0	58.9	20.0	1.4	15.2
M_3 (Quadrupole)	45.5	22.1	11.2	7.4	1.6	13.1
M_4 (Kinematic Direction)	23.8	30.7	24.5	12.9	6.1	13.4
M_5 (Kinematic Velocity)	30.4	27.9	17.7	9.0	5.1	7.4
M_6 (Kinematic Dipole)	16.3	18.4	15.6	11.0	7.1	10.1

Table A.2: As for Table A.1 but with the Poisson statistics.

Hypothesis	Galactic mask angle b°					
	0.0	10.0	20.0	30.0	40.0	30.0*
M_0 (Null)	0.0	0.0	0.0	0.0	0.0	0.0
M_1 (Dipole)	375.9	308.5	146.4	49.6	21.0	18.6
M_2 (Double Dipole)	426.8	329.2	156.4	49.6	20.3	16.3
M_3 (Quadrupole)	64.4	27.5	10.2	1.6	0.0	6.8
M_4 (Kinematic Direction)	32.6	43.2	43.6	29.2	21.3	16.0
M_5 (Kinematic Velocity)	62.9	56.6	37.3	20.9	14.6	11.5
M_6 (Kinematic Dipole)	21.8	25.2	24.5	18.5	14.5	12.6

Table A.3: As for Table A.1 but with Quaia high.

Hypothesis	Galactic mask angle b°					
	0.0	10.0	20.0	30.0	40.0	30.0*
M_0 (Null)	0.0	0.0	0.0	0.0	0.0	0.0
M_1 (Dipole)	376.0	308.1	146.5	49.3	21.2	18.8
M_2 (Double Dipole)	426.8	328.5	155.8	50.9	20.2	16.2
M_3 (Quadrupole)	64.4	27.7	10.2	2.3	0.2	7.2
M_4 (Kinematic Direction)	32.5	43.2	43.6	29.2	21.4	16.3
M_5 (Kinematic Velocity)	63.1	56.5	37.4	20.7	14.9	11.3
M_6 (Kinematic Dipole)	21.9	25.1	24.2	18.6	14.5	12.7

Table A.4: As for Table A.2 but with Quaia high.

Appendix B

Disc masks for RACS and NVSS radio galaxies

Sample	l°	b°	r°	Source
RACS	107.0	-43.0	3.4	-
	79.0	-30.0	"	-
	25.0	26.0	"	Hercules A
	286.7	73.5	"	Virgo A

Table B.1: Centre position (l°, b°) and radius r° of the four distinct disc masks used in RACS. Bright radio sources in the region (if any) are mentioned in the ‘Source’ column.

Sample	l°	b°	r°	Source
NVSS	239.9	-56.6	2.9	Fornax A
	208.0	-16.2	"	Orion A
	222.2	11.1	"	-
	286.2	73.2	"	Virgo A

Table B.2: As for Table B.1 but with NVSS.

Appendix C

Summary of RACS and NVSS radio galaxies

Sample	mJy cut	δ included	Gal. mask	N
RACS(A)	10	$-77^\circ \leq \delta \leq 29^\circ$	$ b \leq 5^\circ$	524 651
RACS(B)	"	"	"	520 885

Table C.1: Summary of final RACS samples, including flux cuts, masking choices and total number of sources. A variant contains the local sources, B variant removes the local sources.

Sample	mJy cut	δ included	Gal. mask	N
NVSS(A)	15	$\delta > -40^\circ$	$ b \leq 10^\circ$	342 308
NVSS(B)	"	"	"	339 425

Table C.2: As for Table C.1 but with NVSS

Appendix D

Table of Bayes Factors for RACS and NVSS radio galaxies

Sample	Model	Log Bayes factor
RACS(A)	M_0 Null	–
	M_1 Free dipole	–0.5
	M_2 Kinematic velocity	3.0
	M_3 Kinematic direction	2.3
	M_4 Kinematic dipole	4.3
RACS(B)	M_0 Null	–
	M_1 Free dipole	–1.9
	M_2 Kinematic velocity	2.1
	M_3 Kinematic direction	0.5
	M_4 Kinematic dipole	3.2

Table D.1: Bayes factors by model for each RACS variant. The highlighted row indicates the model with highest Bayes factor.

Sample	Model	Log Bayes factor
NVSS(A)	M_0 Null	–
	M_1 Free dipole	2.7
	M_2 Kinematic velocity	3.6
	M_3 Kinematic direction	7.1
	M_4 Kinematic dipole	5.1
NVSS(B)	M_0 Null	–
	M_1 Free dipole	–0.2
	M_2 Kinematic velocity	2.6
	M_3 Kinematic direction	4.1
	M_4 Kinematic dipole	4.5

Table D.2: As for Table D.1 but with NVSS

Sample	Model	Log Bayes factor
RACS(B) + NVSS(B)	M_0 Null	—
	M_1 Free dipole	1.6
	M_2 Kinematic velocity	4.8
	M_3 Kinematic direction	4.5
	M_4 Kinematic dipole	7.7

Table D.3: As for Table D.1 but with joint analysis of RACS(B) and NVSS(B).

Bibliography

- [Blake 02] Chris Blake & Jasper Wall. *A velocity dipole in the distribution of radio galaxies.* nat, vol. 416, no. 6877, pages 150–152, March 2002.
- [Cheng 23] Yun-Ting Cheng, Tzu-Ching Chang & Adam Lidz. *Is the Radio Source Dipole from NVSS Consistent with the CMB and Λ CDM?* arXiv e-prints, page arXiv:2309.02490, September 2023.
- [Colin 17] Jacques Colin, Roya Mohayaee, Mohamed Rameez & Subir Sarkar. *High-redshift radio galaxies and divergence from the CMB dipole.* MNRAS, vol. 471, no. 1, pages 1045–1055, October 2017.
- [Condon 98] J. J. Condon, W. D. Cotton, E. W. Greisen, Q. F. Yin, R. A. Perley, G. B. Taylor & J. J. Broderick. *The NRAO VLA Sky Survey.* aj, vol. 115, no. 5, pages 1693–1716, May 1998.
- [Conn 11] A. R. Conn, G. F. Lewis, R. A. Ibata, Q. A. Parker, D. B. Zucker, A. W. McConnachie, N. F. Martin, M. J. Irwin, N. Tanvir, M. A. Fardal & A. M. N. Ferguson. *A Bayesian Approach to Locating the Red Giant Branch Tip Magnitude. I.* apj, vol. 740, no. 2, page 69, October 2011.
- [Conn 12] A. R. Conn, R. A. Ibata, G. F. Lewis, Q. A. Parker, D. B. Zucker, N. F. Martin, A. W. McConnachie, M. J. Irwin, N. Tanvir, M. A. Fardal, A. M. N. Ferguson, S. C. Chapman & D. Valls-Gabaud. *A Bayesian Approach to Locating the Red Giant Branch Tip Magnitude. II. Distances to the Satellites of M31.* apj, vol. 758, no. 1, page 11, October 2012.

- [Dalang 22] Charles Dalang & Camille Bonvin. *On the kinematic cosmic dipole tension*. Monthly Notices of the Royal Astronomical Society, vol. 512, no. 3, pages 3895–3905, 03 2022.
- [Dam 23] Lawrence Dam, Geraint F. Lewis & Brendon J. Brewer. *Testing the cosmological principle with CatWISE quasars: a bayesian analysis of the number-count dipole*. MNRAS, vol. 525, no. 1, pages 231–245, October 2023.
- [Darling 22] Jeremy Darling. *The Universe is Brighter in the Direction of Our Motion: Galaxy Counts and Fluxes are Consistent with the CMB Dipole*. apjl, vol. 931, no. 2, page L14, June 2022.
- [Einstein 17] Albert Einstein. *Cosmological Considerations in the General Theory of Relativity*. Sitzungsber. Preuss. Akad. Wiss. Berlin (Math. Phys.), vol. 1917, pages 142–152, 1917.
- [Ellis 84] G. F. R. Ellis & J. E. Baldwin. *On the expected anisotropy of radio source counts*. MNRAS, vol. 206, pages 377–381, January 1984.
- [European Space Agency 21] European Space Agency & Gaia Data Processing and Analysis Consortium, march 2021.
- [Friedmann 22] A. Friedmann. *Über die Krümmung des Raumes*. Zeitschrift fur Physik, vol. 10, pages 377–386, January 1922.
- [Gaia Collaboration 16] Gaia Collaboration, T. Prusti, J. H. J. de Bruijne, A. G. A. Brown, A. Vallenari, C. Babusiaux, C. A. L. Bailer-Jones, U. Bastian, M. Biermann, D. W. Evans, L. Eyer, F. Jansen, C. Jordi, S. A. Klioner, U. Lammers, L. Lindegren, X. Luri, F. Mignard, D. J. Milligan, C. Panem, V. Poinsignon, D. Pourbaix, S. Randich, G. Sarri, P. Sartoretti, H. I. Siddiqui, C. Soubiran, V. Valette, F. van Leeuwen, N. A. Walton, C. Aerts, F. Arenou, M. Cropper, R. Drimmel, E. Høg, D. Katz, M. G. Lattanzi, W. O'Mullane, E. K. Grebel, A. D. Holland, C. Huc, X. Passot, L. Bramante, C. Cacciari, J. Castañeda, L. Chaoul, N. Cheek, F. De Angeli, C. Fabricius, R. Guerra, J. Hernández, A. Jean-Antoine-Piccolo, E. Masana, R. Messineo, N. Mowlavi, K. Nienartowicz, D. Ordóñez-Blanco, P. Panuzzo, J. Portell, P. J. Richards,

M. Riello, G. M. Seabroke, P. Tanga, F. Thévenin, J. Torra, S. G. Els, G. Gracia-Abril, G. Comoretto, M. Garcia-Reinaldos, T. Lock, E. Mercier, M. Altmann, R. Andrae, T. L. Astraatmadja, I. Bellas-Velidis, K. Benson, J. Berthier, R. Blomme, G. Busso, B. Carry, A. Cellino, G. Clementini, S. Cowell, O. Creevey, J. Cuypers, M. Davidson, J. De Ridder, A. de Torres, L. Delchambre, A. Dell’Oro, C. Ducourant, Y. Frémat, M. García-Torres, E. Gosset, J. L. Halbwachs, N. C. Hambly, D. L. Harrison, M. Hauser, D. Hestroffer, S. T. Hodgkin, H. E. Huckle, A. Hutton, G. Jasniewicz, S. Jordan, M. Kontizas, A. J. Korn, A. C. Lanzafame, M. Manteiga, A. Moitinho, K. Muinonen, J. Osinde, E. Pancino, T. Pauwels, J. M. Petit, A. Recio-Blanco, A. C. Robin, L. M. Sarro, C. Siopis, M. Smith, K. W. Smith, A. Sozzetti, W. Thuillot, W. van Reeven, Y. Viala, U. Abbas, A. Abreu Aramburu, S. Accart, J. J. Aguado, P. M. Allan, W. Allasia, G. Altavilla, M. A. Álvarez, J. Alves, R. I. Anderson, A. H. Andrei, E. Anglada Varela, E. Antiche, T. Antoja, S. Antón, B. Arcay, A. Atzei, L. Ayache, N. Bach, S. G. Baker, L. Balaguer-Núñez, C. Barache, C. Barata, A. Barbier, F. Barblan, M. Baroni, D. Barrado y Navascués, M. Barros, M. A. Barstow, U. Becciani, M. Bellazzini, G. Bellei, A. Bello García, V. Belokurov, P. Bendjoya, A. Berihuete, L. Bianchi, O. Bienaymé, F. Billebaud, N. Blagorodnova, S. Blanco-Cuaresma, T. Boch, A. Bombrun, R. Borrachero, S. Bouquillon, G. Bourda, H. Bouy, A. Bragaglia, M. A. Breddels, N. Brouillet, T. Brüsemeister, B. Bucciarelli, F. Budnik, P. Burgess, R. Burgon, A. Burlacu, D. Busonero, R. Buzzi, E. Caffau, J. Cambras, H. Campbell, R. Cancelliere, T. Cantat-Gaudin, T. Carlucci, J. M. Carrasco, M. Castellani, P. Charlot, J. Charnas, P. Charvet, F. Chassat, A. Chiavassa, M. Clotet, G. Cocozza, R. S. Collins, P. Collins, G. Costigan, F. Crifo, N. J. G. Cross, M. Crosta, C. Crowley, C. Dafonte, Y. Damerdji, A. Daperogolas, P. David, M. David, P. De Cat, F. de Felice, P. de Laverny, F. De Luise, R. De March, D. de Martino, R. de Souza, J. Debosscher, E. del Pozo, M. Delbo, A. Delgado, H. E.

Delgado, F. di Marco, P. Di Matteo, S. Diakite, E. Distefano, C. Dolding, S. Dos Anjos, P. Drazinos, J. Durán, Y. Dzigan, E. Ecale, B. Edvardsson, H. Enke, M. Erdmann, D. Escolar, M. Espina, N. W. Evans, G. Eynard Bontemps, C. Fabre, M. Fabrizio, S. Faigler, A. J. Falcão, M. Farràs Casas, F. Faye, L. Federici, G. Fedorets, J. Fernández-Hernández, P. Fernique, A. Fienga, F. Figueras, F. Filippi, K. Find-eisen, A. Fonti, M. Fouesneau, E. Fraile, M. Fraser, J. Fuchs, R. Furnell, M. Gai, S. Galleti, L. Galluccio, D. Garabato, F. García-Sedano, P. Garé, A. Garofalo, N. Garralda, P. Gavras, J. Gerssen, R. Geyer, G. Gilmore, S. Girona, G. Giuffrida, M. Gomes, A. González-Marcos, J. González-Núñez, J. J. González-Vidal, M. Granvik, A. Guerrier, P. Guillout, J. Guiraud, A. Gúrpide, R. Gutiérrez-Sánchez, L. P. Guy, R. Haigron, D. Hatzidimitriou, M. Haywood, U. Heiter, A. Helmi, D. Hobbs, W. Hofmann, B. Holl, G. Holland, J. A. S. Hunt, A. Hypki, V. Icardi, M. Irwin, G. Jevardat de Fombelle, P. Jofré, P. G. Jonker, A. Jorissen, F. Julbe, A. Karampelas, A. Kochoska, R. Kohley, K. Kollenberg, E. Kontizas, S. E. Koposov, G. Kordopatis, P. Koubsky, A. Kowalczyk, A. Krone-Martins, M. Kudryashova, I. Kull, R. K. Bachchan, F. Lacoste-Seris, A. F. Lanza, J. B. Lavigne, C. Le Poncin-Lafitte, Y. Lebreton, T. Lebzelter, S. Lecchia, N. Leclerc, I. Lecoeur-Taibi, V. Lemaitre, H. Lenhardt, F. Leroux, S. Liao, E. Licata, H. E. P. Lindstrøm, T. A. Lister, E. Livanou, A. Lobel, W. Löffler, M. López, A. Lopez-Lozano, D. Lorenz, T. Loureiro, I. MacDonald, T. Magalhães Fernandes, S. Managau, R. G. Mann, G. Mantlet, O. Marchal, J. M. Marchant, M. Marconi, J. Marie, S. Marinoni, P. M. Marrese, G. Marschalkó, D. J. Marshall, J. M. Martín-Fleitas, M. Martino, N. Mary, G. Matijević, T. Mazeh, P. J. McMillan, S. Messina, A. Mestre, D. Michalik, N. R. Millar, B. M. H. Miranda, D. Molina, R. Molinaro, M. Molinaro, L. Molnár, M. Moniez, P. Montegriffo, D. Monteiro, R. Mor, A. Mora, R. Morbidelli, T. Morel, S. Morgenthaler, T. Morley, D. Morris, A. F. Mulone, T. Muraveva, I. Musella, J. Narbonne, G. Nelemans, L. Nicas-

tro, L. Noval, C. Ordénovic, J. Ordieres-Meré, P. Osborne, C. Pagani, I. Pagano, F. Pailler, H. Palacin, L. Palaversa, P. Parsons, T. Paulsen, M. Pecoraro, R. Pedrosa, H. Pentikäinen, J. Pereira, B. Pichon, A. M. Piersimoni, F. X. Pineau, E. Plachy, G. Plum, E. Poujoulet, A. Prša, L. Pulone, S. Ragaini, S. Rago, N. Rambaux, M. Ramos-Lerate, P. Ranalli, G. Rauw, A. Read, S. Regibo, F. Renk, C. Reylé, R. A. Ribeiro, L. Rimoldini, V. Ripepi, A. Riva, G. Rixon, M. Roelens, M. Romero-Gómez, N. Rowell, F. Royer, A. Rudolph, L. Ruiz-Dern, G. Sadowski, T. Sagristà Sellés, J. Sahlmann, J. Salgado, E. Salguero, M. Sarasso, H. Savietto, A. Schnorhk, M. Schultheis, E. Sciacca, M. Segol, J. C. Segovia, D. Segransan, E. Serpell, I. C. Shih, R. Smareglia, R. L. Smart, C. Smith, E. Solano, F. Solitro, R. Sordo, S. Soria Nieto, J. Souchay, A. Spagna, F. Spoto, U. Stampa, I. A. Steele, H. Steidelmüller, C. A. Stephenson, H. Stoev, F. F. Suess, M. Süveges, J. Surdej, L. Szabados, E. Szegedi-Elek, D. Tapiador, F. Taris, G. Tauran, M. B. Taylor, R. Teixeira, D. Terrett, B. Tingley, S. C. Trager, C. Turon, A. Ulla, E. Utrilla, G. Valentini, A. van Elteren, E. Van Hemelryck, M. van Leeuwen, M. Varadi, A. Vecchiato, J. Veljanoski, T. Via, D. Vicente, S. Vogt, H. Voss, V. Votruba, S. Voutsinas, G. Walmsley, M. Weiler, K. Weingrill, D. Werner, T. Wevers, G. Whitehead, Ł. Wyrzykowski, A. Yoldas, M. Žerjal, S. Zucker, C. Zurbach, T. Zwitter, A. Alecu, M. Allen, C. Allende Prieto, A. Amorim, G. Anglada-Escudé, V. Arsenijevic, S. Azaz, P. Balm, M. Beck, H. H. Bernstein, L. Bigot, A. Bijaoui, C. Blasco, M. Bonfigli, G. Bono, S. Boudreault, A. Bressan, S. Brown, P. M. Brunet, P. Bunclark, R. Buonanno, A. G. Butkevich, C. Carré, C. Carrion, L. Chemin, F. Chéreau, L. Corcione, E. Darmigny, K. S. de Boer, P. de Teodoro, P. T. de Zeeuw, C. Delle Luche, C. D. Domingues, P. Dubath, F. Fodor, B. Frézouls, A. Fries, D. Fustes, D. Fyfe, E. Gallardo, J. Gallegos, D. Gardiol, M. Gebran, A. Gomboc, A. Gómez, E. Grux, A. Gueguen, A. Heyrovsky, J. Hoar, G. Iannicola, Y. Isasi Parache, A. M. Janotto, E. Joliet, A. Jonck-

heere, R. Keil, D. W. Kim, P. Klagyivik, J. Klar, J. Knude, O. Kochukhov, I. Kolka, J. Kos, A. Kutka, V. Lainey, D. LeBouquin, C. Liu, D. Loreggia, V. V. Makarov, M. G. Marseille, C. Martayan, O. Martinez-Rubi, B. Massart, F. Meynadier, S. Mignot, U. Munari, A. T. Nguyen, T. Nordlander, P. Ocvirk, K. S. O'Flaherty, A. Olias Sanz, P. Ortiz, J. Osorio, D. Oszkiewicz, A. Ouzounis, M. Palmer, P. Park, E. Pasquato, C. Peltzer, J. Peralta, F. Péturaud, T. Pieniluoma, E. Pigozzi, J. Poels, G. Prat, T. Prod'homme, F. Raison, J. M. Rebordao, D. Risquez, B. Rocca-Volmerange, S. Rosen, M. I. Ruiz-Fuertes, F. Russo, S. Sembay, I. Serraller Vizcaino, A. Short, A. Siebert, H. Silva, D. Sina-chopoulos, E. Slezak, M. Soffel, D. Sosnowska, V. Stražys, M. ter Linden, D. Terrell, S. Theil, C. Tiede, L. Troisi, P. Tsalmantza, D. Tur, M. Vaccari, F. Vachier, P. Valles, W. Van Hamme, L. Veltz, J. Virtanen, J. M. Wallut, R. Wichmann, M. I. Wilkinson, H. Ziaeepour & S. Zschocke. *The Gaia mission.* aap, vol. 595, page A1, November 2016.

[Gaia Collaboration 23a]

Gaia Collaboration, C. A. L. Bailer-Jones, D. Teyssier, L. Delchambre, C. Ducourant, D. Garabato, D. Hatzidimitriou, S. A. Klioner, L. Rimoldini, I. Bellas-Velidis, R. Carballo, M. I. Carnerero, C. Diener, M. Fouesneau, L. Galluccio, P. Gavras, A. Krone-Martins, C. M. Raiteri, R. Teixeira, A. G. A. Brown, A. Vallenari, T. Prusti, J. H. J. de Bruijne, F. Arenou, C. Babusiaux, M. Biermann, O. L. Creevey, D. W. Evans, L. Eyer, R. Guerra, A. Hutton, C. Jordi, U. L. Lammers, L. Lindegren, X. Luri, F. Mignard, C. Panem, D. Pourbaix, S. Randich, P. Sartoretti, C. Soubiran, P. Tanga, N. A. Walton, U. Bastian, R. Drimmel, F. Jansen, D. Katz, M. G. Lattanzi, F. van Leeuwen, J. Bakker, C. Cacciari, J. Castañeda, F. De Angeli, C. Fabricius, Y. Frémat, A. Guerrier, U. Heiter, E. Masana, R. Messineo, N. Mowlavi, C. Nicolas, K. Nienartowicz, F. Pailler, P. Panuzzo, F. Riclet, W. Roux, G. M. Seabroke, R. Sordo, F. Thévenin, G. Gracia-Abril, J. Portell, M. Altmann, R. Andrae, M. Audard, K. Benson, J. Berthier, R. Blomme, P. W. Burgess, D. Busonero, G. Busso, H. Cánovas, B. Carry, A. Cellino,

N. Cheek, G. Clementini, Y. Damerdji, M. Davidson, P. de Teodoro, M. Nuñez Campos, A. Dell’Oro, P. Esquej, J. Fernández-Hernández, E. Fraile, P. García-Lario, E. Gosset, R. Haigron, J. L. Halbwachs, N. C. Hambly, D. L. Harrison, J. Hernández, D. Hestroffer, S. T. Hodgkin, B. Holl, K. Janßen, G. Jevardat de Fombelle, S. Jordan, A. C. Lanzafame, W. Löffler, O. Marchal, P. M. Marrese, A. Moitinho, K. Muinonen, P. Osborne, E. Pancino, T. Pauwels, A. Recio-Blanco, C. Reylé, M. Riello, T. Roegiers, J. Rybizki, L. M. Sarro, C. Siopsis, M. Smith, A. Sozzetti, E. Utrilla, M. van Leeuwen, U. Abbas, P. Ábrahám, A. Abreu Aramburu, C. Aerts, J. J. Aguado, M. Ajaj, F. Aldea-Montero, G. Altavilla, M. A. Álvarez, J. Alves, R. I. Anderson, E. Anglada Varela, T. Antoja, D. Baines, S. G. Baker, L. Balaguer-Núñez, E. Balbinot, Z. Balog, C. Barache, D. Barbato, M. Barros, M. A. Barstow, S. Bartolomé, J. L. Bassiliana, N. Bauchet, U. Becciani, M. Bellazzini, A. Berihuete, M. Bernet, S. Bertone, L. Bianchi, A. Binnenfeld, S. Blanco-Cuaresma, T. Boch, A. Bombrun, D. Bossini, S. Bouquillon, A. Bragaglia, L. Bramante, E. Breedt, A. Bressan, N. Brouillet, E. Brugaletta, B. Bucciarelli, A. Burlacu, A. G. Butkevich, R. Buzzi, E. Caffau, R. Cancelliere, T. Cantat-Gaudin, T. Carlucci, J. M. Carrasco, L. Casamiquela, M. Castellani, A. Castro-Ginard, L. Chaoul, P. Charlot, L. Chemin, V. Chiaramida, A. Chiavassa, N. Chornay, G. Comoretto, G. Contursi, W. J. Cooper, T. Cornez, S. Cowell, F. Crifo, M. Cropper, M. Crosta, C. Crowley, C. Dafonte, A. Dapergolas, P. David, P. de Laverny, F. De Luise, R. De March, J. De Ridder, R. de Souza, A. de Torres, E. F. del Peloso, E. del Pozo, M. Delbo, A. Delgado, J. B. Delisle, C. Demouchy, T. E. Dharmawardena, S. Diakite, E. Distefano, C. Dolding, H. Enke, C. Fabre, M. Fabrizio, S. Faigler, G. Fedorets, P. Fernique, F. Figueras, Y. Fournier, C. Fouron, F. Frakoudi, M. Gai, A. Garcia-Gutierrez, M. Garcia-Reinaldos, M. García-Torres, A. Garofalo, A. Gavel, E. Gerlach, R. Geyer, P. Giacobbe, G. Gilmore, S. Girona, G. Giufrida, R. Gomel, A. Gomez, J. González-Núñez, I. González-

Santamaría, J. J. González-Vidal, M. Granvik, P. Guillout, J. Guiraud, R. Gutiérrez-Sánchez, L. P. Guy, M. Hauser, M. Haywood, A. Helmer, A. Helmi, M. H. Sarmiento, S. L. Hidalgo, T. Hilger, N. Hładczuk, D. Hobbs, G. Holland, H. E. Huckle, K. Jardine, G. Jasniewicz, A. Jean-Antoine Piccolo, Ó. Jiménez-Arranz, J. Juaristi Campillo, F. Julbe, L. Karbevska, P. Kervella, S. Khanna, M. Kontizas, G. Kordopatis, A. J. Korn, Á. Kóspál, Z. Kostrzewska-Rutkowska, K. Kruszyńska, M. Kun, P. Laizeau, S. Lambert, A. F. Lanza, Y. Lasne, J. F. Le Campion, Y. Lebreton, T. Lebzelter, S. Leccia, N. Leclerc, I. Lecoeur-Taibi, S. Liao, E. L. Licata, H. E. P. Lindstrøm, T. A. Lister, E. Livanou, A. Lobel, A. Lorca, C. Loup, P. Madrero Pardo, A. Magdaleno Romeo, S. Managau, R. G. Mann, M. Manteiga, J. M. Marchant, M. Marconi, J. Marcos, M. M. S. Marcos Santos, D. Marín Pina, S. Marinoni, F. Marocco, D. J. Marshall, L. Martin Polo, J. M. Martín-Fleitas, G. Marton, N. Mary, A. Masip, D. Massari, A. Mastrobuono-Battisti, T. Mazeh, P. J. McMillan, S. Messina, D. Michalik, N. R. Millar, A. Mints, D. Molina, R. Molinaro, L. Molnár, G. Monari, M. Monguió, P. Montegriffo, A. Montero, R. Mor, A. Mora, R. Morbidelli, T. Morel, D. Morris, T. Muraveva, C. P. Murphy, I. Musella, Z. Nagy, L. Noval, F. Ocaña, A. Ogden, C. Ordenovic, J. O. Osinde, C. Pagani, I. Pagano, L. Palaversa, P. A. Palicio, L. Pallas-Quintela, A. Panahi, S. Payne-Wardenaar, X. Peñalosa Esteller, A. Penttilä, B. Pi-chon, A. M. Piersimoni, F. X. Pineau, E. Plachy, G. Plum, E. Poggio, A. Prša, L. Pulone, E. Racero, S. Ragaini, M. Rainer, P. Ramos, M. Ramos-Lerate, P. Re Fiorentin, S. Regibo, P. J. Richards, C. Rios Diaz, V. Ripepi, A. Riva, H. W. Rix, G. Rixon, N. Robichon, A. C. Robin, C. Robin, M. Roelens, H. R. O. Rogues, L. Rohrbasser, M. Romero-Gómez, N. Rowell, F. Royer, D. Ruz Mieres, K. A. Rybicki, G. Sadowski, A. Sáez Núñez, A. Sagristà Sellés, J. Sahlmann, E. Salguero, N. Samaras, V. Sanchez Gimenez, N. Sanna, R. Santoveña, M. Sarasso, M. Schultheis, E. Sciacca, M. Segol, J. C. Segovia, D. Ségransan, D. Semeux,

S. Shahaf, H. I. Siddiqui, A. Siebert, L. Siltala, A. Silvelo, E. Slezak, I. Slezak, R. L. Smart, O. N. Snaith, E. Solano, F. Solitro, D. Souami, J. Souchay, A. Spagna, L. Spina, F. Spoto, I. A. Steele, H. Steidelmüller, C. A. Stephenson, M. Süveges, J. Surdej, L. Szabados, E. Szegedi-Elek, F. Taris, M. B. Taylor, L. Tolomei, N. Tonello, F. Torra, J. Torra, G. Torralba Elipe, M. Trabucchi, A. T. Tsounis, C. Turon, A. Ulla, N. Unger, M. V. Vaillant, E. van Dillen, W. van Reeven, O. Vanel, A. Vecchiato, Y. Viala, D. Vicente, S. Voutsinas, M. Weiler, T. Wevers, Ł. Wyrzykowski, A. Yoldas, P. Yvard, H. Zhao, J. Zorec, S. Zucker & T. Zwitter. *Gaia Data Release 3. The extragalactic content.* aap, vol. 674, page A41, June 2023.

[Gaia Collaboration 23b]

Gaia Collaboration, A. Vallenari, A. G. A. Brown, T. Prusti, J. H. J. de Bruijne, F. Arenou, C. Babusiaux, M. Biermann, O. L. Creevey, C. Ducourant, D. W. Evans, L. Eyer, R. Guerra, A. Hutton, C. Jordi, S. A. Klioner, U. L. Lammers, L. Lindegren, X. Luri, F. Mignard, C. Panem, D. Pourbaix, S. Randich, P. Sartoretti, C. Soubiran, P. Tanga, N. A. Walton, C. A. L. Bailer-Jones, U. Bastian, R. Drimmel, F. Jansen, D. Katz, M. G. Lattanzi, F. van Leeuwen, J. Bakker, C. Cacciari, J. Castañeda, F. De Angeli, C. Fabricius, M. Fouesneau, Y. Frémat, L. Galluccio, A. Guerrier, U. Heiter, E. Masana, R. Messineo, N. Mowlavi, C. Nicolas, K. Nienartowicz, F. Pailler, P. Panuzzo, F. Rizlet, W. Roux, G. M. Seabroke, R. Sordo, F. Thévenin, G. Gracia-Abril, J. Portell, D. Teyssier, M. Altmann, R. Andrae, M. Audard, I. Bellas-Velidis, K. Benson, J. Berthier, R. Blomme, P. W. Burgess, D. Busonero, G. Busso, H. Cánovas, B. Carry, A. Cellino, N. Cheek, G. Clementini, Y. Damerdji, M. Davidson, P. de Teodoro, M. Nuñez Campos, L. Delchambre, A. Dell’Oro, P. Esquej, J. Fernández-Hernández, E. Fraile, D. Garabato, P. García-Lario, E. Gosset, R. Haigron, J. L. Halbwachs, N. C. Hambly, D. L. Harrison, J. Hernández, D. Hestroffer, S. T. Hodgkin, B. Holl, K. Janßen, G. Jevardat de Fombelle, S. Jordan, A. Krone-Martins, A. C. Lanzafame, W. Löffler, O. Marchal, P. M.

Marrese, A. Moitinho, K. Muinonen, P. Osborne, E. Pancino, T. Pauwels, A. Recio-Blanco, C. Reylé, M. Riello, L. Rimoldini, T. Roegiers, J. Rybizki, L. M. Sarro, C. Siopsis, M. Smith, A. Sozzetti, E. Utrilla, M. van Leeuwen, U. Abbas, P. Ábrahám, A. Abreu Aramburu, C. Aerts, J. J. Aguado, M. Ajaj, F. Aldea-Montero, G. Altavilla, M. A. Álvarez, J. Alves, F. Anders, R. I. Anderson, E. Anglada Varela, T. Antoja, D. Baines, S. G. Baker, L. Balaguer-Núñez, E. Balbinot, Z. Balog, C. Barache, D. Barbato, M. Barros, M. A. Barstow, S. Bartolomé, J. L. Bassiliana, N. Bauchet, U. Becciani, M. Bellazzini, A. Berihuete, M. Bernet, S. Bertone, L. Bianchi, A. Binnenfeld, S. Blanco-Cuaresma, A. Blazere, T. Boch, A. Bombrun, D. Bossini, S. Bouquillon, A. Bragaglia, L. Bramante, E. Breedt, A. Bressan, N. Brouillet, E. Brugaletta, B. Bucciarelli, A. Burlacu, A. G. Butkevich, R. Buzzi, E. Cafau, R. Cancelliere, T. Cantat-Gaudin, R. Carballo, T. Carrucci, M. I. Carnerero, J. M. Carrasco, L. Casamiquela, M. Castellani, A. Castro-Ginard, L. Chaoul, P. Charlot, L. Chemin, V. Chiaramida, A. Chiavassa, N. Chornay, G. Comoretto, G. Contursi, W. J. Cooper, T. Cornez, S. Cowell, F. Crifo, M. Cropper, M. Crosta, C. Crowley, C. Dafonte, A. Dapergolas, M. David, P. David, P. de Laverny, F. De Luise, R. De March, J. De Ridder, R. de Souza, A. de Torres, E. F. del Peloso, E. del Pozo, M. Delbo, A. Delgado, J. B. Delisle, C. Demouchy, T. E. Dharmawardena, P. Di Matteo, S. Diakite, C. Diener, E. Distefano, C. Dolding, B. Edvardsson, H. Enke, C. Fabre, M. Fabrizio, S. Faigler, G. Fedorets, P. Fernique, A. Fienga, F. Figueras, Y. Fournier, C. Fouron, F. Frakoudi, M. Gai, A. Garcia-Gutierrez, M. Garcia-Reinaldos, M. García-Torres, A. Garofalo, A. Gavel, P. Gavras, E. Gerlach, R. Geyer, P. Giacobbe, G. Gilmore, S. Girona, G. Giuffrida, R. Gomel, A. Gomez, J. González-Núñez, I. González-Santamaría, J. J. González-Vidal, M. Granvik, P. Guillout, J. Guiraud, R. Gutiérrez-Sánchez, L. P. Guy, D. Hatzidimitriou, M. Hauser, M. Haywood, A. Helmer, A. Helmi, M. H. Sarmiento, S. L. Hi-

dalgo, T. Hilger, N. Hładcuk, D. Hobbs, G. Holland, H. E. Huckle, K. Jardine, G. Jasniewicz, A. Jean-Antoine Piccolo, Ó. Jiménez-Arranz, A. Jorissen, J. Juaristi Campillo, F. Julbe, L. Karbevska, P. Kervella, S. Khanna, M. Kontizas, G. Kordopatis, A. J. Korn, Á. Kóspál, Z. Kostrzewska-Rutkowska, K. Kruszyńska, M. Kun, P. Laizeau, S. Lambert, A. F. Lanza, Y. Lasne, J. F. Le Campion, Y. Lebretton, T. Lebzelter, S. Leccia, N. Leclerc, I. Lecoeur-Taibi, S. Liao, E. L. Licata, H. E. P. Lindstrøm, T. A. Lister, E. Livianou, A. Lobel, A. Lorca, C. Loup, P. Madrero Pardo, A. Magdaleno Romeo, S. Managau, R. G. Mann, M. Manteiga, J. M. Marchant, M. Marconi, J. Marcos, M. M. S. Marcos Santos, D. Marín Pina, S. Marinoni, F. Marocco, D. J. Marshall, L. Martin Polo, J. M. Martín-Fleitas, G. Marton, N. Mary, A. Masip, D. Massari, A. Mastrobuono-Battisti, T. Mazeh, P. J. McMillan, S. Messina, D. Michalik, N. R. Millar, A. Mints, D. Molina, R. Molinaro, L. Molnár, G. Monari, M. Monguió, P. Montegriffo, A. Montero, R. Mor, A. Mora, R. Morbidelli, T. Morel, D. Morris, T. Muraveva, C. P. Murphy, I. Musella, Z. Nagy, L. Noval, F. Ocaña, A. Ogden, C. Ordenovic, J. O. Osinde, C. Pagani, I. Pagano, L. Palaversa, P. A. Palicio, L. Pallas-Quintela, A. Panahi, S. Payne-Wardenaar, X. Peñalosa Esteller, A. Penttilä, B. Pichon, A. M. Piersimoni, F. X. Pineau, E. Plachy, G. Plum, E. Poggio, A. Prša, L. Pulone, E. Racero, S. Ragaini, M. Rainer, C. M. Raiteri, N. Rambaux, P. Ramos, M. Ramos-Lerate, P. Re Fiorentin, S. Regibo, P. J. Richards, C. Rios Diaz, V. Ripepi, A. Riva, H. W. Rix, G. Rixon, N. Robichon, A. C. Robin, C. Robin, M. Roelens, H. R. O. Rogues, L. Rohrbasser, M. Romero-Gómez, N. Rowell, F. Royer, D. Ruz Mieres, K. A. Rybicki, G. Sadowski, A. Sáez Núñez, A. Sagristà Sellés, J. Sahlmann, E. Salguero, N. Samaras, V. Sanchez Gimenez, N. Sanna, R. Santoveña, M. Sarasso, M. Schultheis, E. Sciacca, M. Segol, J. C. Segovia, D. Ségransan, D. Semeux, S. Shahaf, H. I. Siddiqui, A. Siebert, L. Siltala, A. Silvelo, E. Slezak, I. Slezak, R. L. Smart, O. N. Snaith, E. Solano,

F. Solitro, D. Souami, J. Souchay, A. Spagna, L. Spina, F. Spoto, I. A. Steele, H. Steidelmüller, C. A. Stephenson, M. Süveges, J. Surdej, L. Szabados, E. Szegedi-Elek, F. Taris, M. B. Taylor, R. Teixeira, L. Tolomei, N. Tonello, F. Torra, J. Torra, G. Torralba Elipe, M. Trabucchi, A. T. Tsounis, C. Turon, A. Ulla, N. Unger, M. V. Vaillant, E. van Dillen, W. van Reeven, O. Vanel, A. Vecchiato, Y. Viala, D. Vicente, S. Voutsinas, M. Weiler, T. Wevers, Ł. Wyrzykowski, A. Yoldas, P. Yvard, H. Zhao, J. Zorec, S. Zucker & T. Zwitter. *Gaia Data Release 3. Summary of the content and survey properties.* aap, vol. 674, page A1, June 2023.

[Gibelyou 12]

Cameron Gibelyou & Dragan Huterer. *Dipoles in the sky.* MNRAS, vol. 427, no. 3, pages 1994–2021, December 2012.

[Górski 05]

K. M. Górski, E. Hivon, A. J. Banday, B. D. Wandelt, F. K. Hansen, M. Reinecke & M. Bartelmann. *HEALPix: A Framework for High-Resolution Discretization and Fast Analysis of Data Distributed on the Sphere.* apj, vol. 622, pages 759–771, April 2005.

[Hale 21]

Catherine L. Hale, D. McConnell, A. J. M. Thomson, E. Lenc, G. H. Heald, A. W. Hotan, J. K. Leung, V. A. Moss, T. Murphy, J. Pritchard, E. M. Sadler, A. J. Stewart & M. T. Whiting. *The Rapid ASKAP Continuum Survey Paper II: First Stokes I Source Catalogue Data Release.* pasa, vol. 38, page e058, November 2021.

[Harrison 00]

E. R. Harrison. *Cosmology. The science of the universe.* Cambridge University Press, 2000.

[Huchra 12]

John P. Huchra, Lucas M. Macri, Karen L. Masters, Thomas H. Jarrett, Perry Berlind, Michael Calkins, Aidan C. Crook, Roc Cutri, Pirin Erdoğdu, Emilio Falco, Teddy George, Conrad M. Hutcheson, Ofer Lahav, Jeff Mader, Jessica D. Mink, Nathalie Martimbeau, Stephen Schneider, Michael Skrutskie, Susan Tokarz & Michael Westover. *The 2MASS Redshift Survey—Description and Data Release.* apjs, vol. 199, no. 2, page 26, April 2012.

- [Kothari 22] Rahul Kothari, Mohit Panwar, Gurmeet Singh, Prabhakar Tiwari & Pankaj Jain. *A study of Dipolar Signal in distant Quasars with various observables*. arXiv e-prints, page arXiv:2208.14397, August 2022.
- [Kumar Aluri 23] Pavan Kumar Aluri, Paolo Cea, Pravabati Chingangbam, Ming-Chung Chu, Roger G. Clowes, Damien Hutsemékers, Joby P. Kochappan, Alexia M. Lopez, Lang Liu, Niels C. M. Martens, C. J. A. P. Martins, Konstantinos Migkas, Eoin Ó Colgáin, Pratyush Pranav, Lior Shamir, Ashok K. Singal, M. M. Sheikh-Jabbari, Jenny Wagner, Shao-Jiang Wang, David L. Wiltshire, Shek Yeung, Lu Yin & Wen Zhao. *Is the observable Universe consistent with the cosmological principle?* Classical and Quantum Gravity, vol. 40, no. 9, page 094001, May 2023.
- [Lemaître 31] Abbé G. Lemaître. *A Homogeneous Universe of Constant Mass and Increasing Radius accounting for the Radial Velocity of Extra-galactic Nebulæ*. Monthly Notices of the Royal Astronomical Society, vol. 91, no. 5, pages 483–490, 03 1931.
- [Mackay 03] David J. C. Mackay. Information Theory, Inference and Learning Algorithms. Cambridge University Press, 2003.
- [Marocco 21] Federico Marocco, Peter R. M. Eisenhardt, John W. Fowler, J. Davy Kirkpatrick, Aaron M. Meisner, Edward F. Schlaflly, S. A. Stanford, Nelson Garcia, Dan Caselden, Michael C. Cushing, Roc M. Cutri, Jacqueline K. Faherty, Christopher R. Gelino, Anthony H. Gonzalez, Thomas H. Jarrett, Renata Koontz, Amanda Mainzer, Elijah J. Marchese, Bahram Mobasher, David J. Schlegel, Daniel Stern, Harry I. Teplitz & Edward L. Wright. *The CatWISE2020 Catalog*. apjs, vol. 253, no. 1, page 8, March 2021.
- [Mauch 03] T. Mauch, T. Murphy, H. J. Buttery, J. Curran, R. W. Hunstead, B. Pietrzynski, J. G. Robertson & E. M. Sadler. *SUMSS: a wide-field radio imaging survey of the southern sky - II. The source catalogue*. MNRAS, vol. 342, no. 4, pages 1117–1130, July 2003.

- [Milne 35] Edward A. Milne. Relativity, gravitation and world-structure. Oxford University Press, 1935.
- [Mittal 24] Vasudev Mittal, Oliver T. Oayda & Geraint F. Lewis. *The cosmic dipole in the Quaia sample of quasars: a Bayesian analysis*. MNRAS, vol. 527, no. 3, pages 8497–8510, January 2024.
- [Newton 87] Isaac Newton. Philosophiæ Naturalis Principia Mathematica. England, 1687.
- [Peebles 22] P.J.E. Peebles. *Anomalies in physical cosmology*. Annals of Physics, vol. 447, page 169159, dec 2022.
- [Planck Collaboration 20] Planck Collaboration, N. Aghanim, Y. Akrami, F. Arroja, M. Ashdown, J. Aumont, C. Baccigalupi, M. Ballardini, A. J. Banday, R. B. Barreiro, N. Bartolo, S. Basak, R. Battye, K. Benabed, J. P. Bernard, M. Bersanelli, P. Bielewicz, J. J. Bock, J. R. Bond, J. Borrill, F. R. Bouchet, F. Boulanger, M. Bucher, C. Burigana, R. C. Butler, E. Calabrese, J. F. Cardoso, J. Carron, B. Casaponsa, A. Challinor, H. C. Chiang, L. P. L. Colombo, C. Combet, D. Contreras, B. P. Crill, F. Cuttaia, P. de Bernardis, G. de Zotti, J. Delabrouille, J. M. Delouis, F. X. Désert, E. Di Valentino, C. Dickinson, J. M. Diego, S. Donzelli, O. Doré, M. Doussis, A. Ducout, X. Dupac, G. Efstathiou, F. Elsner, T. A. Enßlin, H. K. Eriksson, E. Falgarone, Y. Fantaye, J. Fergusson, R. Fernandez-Cobos, F. Finelli, F. Forastieri, M. Frailis, E. Franceschi, A. Frolov, S. Galeotta, S. Galli, K. Ganga, R. T. Génova-Santos, M. Gerbino, T. Ghosh, J. González-Nuevo, K. M. Górski, S. Gratton, A. Gruppuso, J. E. Gudmundsson, J. Hamann, W. Handley, F. K. Hansen, G. Helou, D. Herranz, S. R. Hildebrandt, E. Hivon, Z. Huang, A. H. Jaffe, W. C. Jones, A. Karakci, E. Keihänen, R. Keskitalo, K. Kiiveri, J. Kim, T. S. Kisner, L. Knox, N. Krachmalnicoff, M. Kunz, H. Kurki-Suonio, G. Lagache, J. M. Lamarre, M. Langer, A. Lasenby, M. Lattanzi, C. R. Lawrence, M. Le Jeune, J. P. Leahy, J. Lesgourges, F. Levrier, A. Lewis, M. Liguori, P. B. Lilje, M. Lilley, V. Lindholm, M. López-Caniego, P. M.

Lubin, Y. Z. Ma, J. F. Macías-Pérez, G. Maggio, D. Maino, N. Mandolesi, A. Mangilli, A. Marcos-Caballero, M. Maris, P. G. Martin, M. Martinelli, E. Martínez-González, S. Matarrese, N. Mauri, J. D. McEwen, P. D. Meerburg, P. R. Meinhold, A. Melchiorri, A. Mennella, M. Migliaccio, M. Millea, S. Mitra, M. A. Miville-Deschénes, D. Molinari, A. Moneti, L. Montier, G. Morgante, A. Moss, S. Mottet, M. Münchmeyer, P. Natoli, H. U. Nørgaard-Nielsen, C. A. Oxborrow, L. Pagano, D. Paoletti, B. Partridge, G. Patanchon, T. J. Pearson, M. Peel, H. V. Peiris, F. Perrotta, V. Pettorino, F. Piacentini, L. Polastri, G. Polenta, J. L. Puget, J. P. Rachen, M. Reinecke, M. Remazeilles, C. Renault, A. Renzi, G. Rocha, C. Rosset, G. Roudier, J. A. Rubiño-Martín, B. Ruiz-Granados, L. Salvati, M. Sandri, M. Savainen, D. Scott, E. P. S. Shellard, M. Shiraishi, C. Sirignano, G. Sirri, L. D. Spencer, R. Sunyaev, A. S. Suur-Uski, J. A. Tauber, D. Tavagnacco, M. Tenti, L. Terenzi, L. Toffolatti, M. Tomasi, T. Trombetti, J. Valiviita, B. Van Tent, L. Vibert, P. Vielva, F. Villa, N. Vittorio, B. D. Wandelt, I. K. Wehus, M. White, S. D. M. White, A. Zacchei & A. Zonca. *Planck 2018 results. I. Overview and the cosmological legacy of Planck*. aap, vol. 641, page A1, September 2020.

[Riello 21]

M. Riello, F. De Angeli, D. W. Evans, P. Montegriffo, J. M. Carrasco, G. Busso, L. Palaversa, P. W. Burgess, C. Diener, M. Davidson, N. Rowell, C. Fabricius, C. Jordi, M. Bellazzini, E. Pancino, D. L. Harrison, C. Cacciari, F. van Leeuwen, N. C. Hambly, S. T. Hodgkin, P. J. Osborne, G. Altavilla, M. A. Barstow, A. G. A. Brown, M. Castellani, S. Cowell, F. De Luise, G. Gilmore, G. Giuffrida, S. Hidalgo, G. Holland, S. Marinoni, C. Pagani, A. M. Piersimoni, L. Pulone, S. Ragagni, M. Rainer, P. J. Richards, N. Sanna, N. A. Walton, M. Weiler & A. Yoldas. *Gaia Early Data Release 3. Photometric content and validation*. aap, vol. 649, page A3, May 2021.

[Robertson 35]

H. P. Robertson. *Kinematics and World-Structure*. ApJ, vol. 82, page 284, November 1935.

- [Rubart 13] M. Rubart & D. J. Schwarz. *Cosmic radio dipole from NVSS and WENSS*. aap, vol. 555, page A117, jul 2013.
- [Scrimgeour 12] Morag I. Scrimgeour, Tamara Davis, Chris Blake, J. Be- rian James, Gregory B. Poole, Lister Staveley-Smith, Sarah Brough, Matthew Colless, Carlos Contreras, Warrick Couch, Scott Croom, Darren Croton, Michael J. Drinkwater, Karl Forster, David Gilbank, Mike Gladders, Karl Glazebrook, Ben Jelliffe, Russell J. Jurek, I. hui Li, Barry Madore, D. Christopher Martin, Kevin Pimbblet, Michael Pracy, Rob Sharp, Emily Wisnioski, David Woods, Ted K. Wyder & H. K. C. Yee. *The WiggleZ Dark Energy Survey: the transition to large-scale cosmic homogeneity*. mnras:, vol. 425, no. 1, pages 116–134, September 2012.
- [Secrest 21] Nathan J. Secrest, Sebastian von Hausegger, Mohamed Rameez, Roya Mohayaee, Subir Sarkar & Jacques Colin. *A Test of the Cosmological Principle with Quasars*. apjl, vol. 908, no. 2, page L51, February 2021.
- [Secrest 22] Nathan J. Secrest, Sebastian von Hausegger, Mohamed Rameez, Roya Mohayaee & Subir Sarkar. *A Challenge to the Standard Cosmological Model*. apjl, vol. 937, no. 2, page L31, October 2022.
- [Siewert 21] Thilo M. Siewert, Matthias Schmidt-Rubart & Dominik J. Schwarz. *Cosmic radio dipole: Estimators and frequency dependence*. aap, vol. 653, page A9, 2021.
- [Singal 11] Ashok K. Singal. *LARGE PECULIAR MOTION OF THE SOLAR SYSTEM FROM THE DIPOLE ANISOTROPY IN SKY BRIGHTNESS DUE TO DISTANT RADIO SOURCES*. The Astrophysical Journal Letters, vol. 742, no. 2, page L23, nov 2011.
- [Singal 21] Ashok K. Singal. *Our Peculiar Motion Inferred from Number Counts of Mid Infra Red AGNs and the Discordance Seen with the Cosmological Principle*. Universe, vol. 7, no. 4, 2021.

- [Singal 23] Ashok K. Singal. *Discordance of dipole asymmetries seen in recent large radio surveys with the cosmological principle*. MNRAS, vol. 524, no. 3, pages 3636–3646, September 2023.
- [Skilling 04] John Skilling. *Nested Sampling*. In Rainer Fischer, Roland Preuss & Udo Von Toussaint, éditeurs, Bayesian Inference and Maximum Entropy Methods in Science and Engineering: 24th International Workshop on Bayesian Inference and Maximum Entropy Methods in Science and Engineering, volume 735 of *American Institute of Physics Conference Series*, pages 395–405, November 2004.
- [Skilling 06] John Skilling. *Nested sampling for general Bayesian computation*. Bayesian Analysis, vol. 1, no. 4, pages 833 – 859, 2006.
- [Speagle 20] Joshua S. Speagle. *DYNESTY: a dynamic nested sampling package for estimating Bayesian posteriors and evidences*. MNRAS, vol. 493, no. 3, pages 3132–3158, April 2020.
- [Storey-Fisher 23] Kate Storey-Fisher, David W. Hogg, Hans-Walter Rix, Anna-Christina Eilers, Giulio Fabbian, Michael Blanton & David Alonso. *Quaia, the Gaia-unWISE Quasar Catalog: An All-Sky Spectroscopic Quasar Sample*. arXiv e-prints, page arXiv:2306.17749, June 2023.
- [Tiwari 16] Prabhakar Tiwari & Adi Nusser. *Revisiting the NVSS number count dipole*. Journal of Cosmology and Astroparticle Physics, vol. 2016, no. 03, page 062, mar 2016.
- [Wagenveld 23] J. D. Wagenveld, H.-R. Klöckner & D. J. Schwarz. *The cosmic radio dipole: Bayesian estimators on new and old radio surveys*. A&A, vol. 675, page A72, 2023.
- [Weinberg 08] Steven Weinberg. Cosmology. 2008.
- [Wright 10] Edward L. Wright, Peter R. M. Eisenhardt, Amy K. Mainzer, Michael E. Ressler, Roc M. Cutri, Thomas Jarrett, J. Davy Kirkpatrick, Deborah Padgett, Robert S. McMillan, Michael Skrutskie, S. A. Stanford, Martin Cohen, Russell G. Walker,

John C. Mather, David Leisawitz, III Gautier Thomas N., Ian McLean, Dominic Benford, Carol J. Lonsdale, Andrew Blain, Bryan Mendez, William R. Irace, Valerie Duvall, Fengchuan Liu, Don Royer, Ingolf Heinrichsen, Joan Howard, Mark Shannon, Martha Kendall, Amy L. Walsh, Mark Larsen, Joel G. Cardon, Scott Schick, Mark Schwalm, Mohamed Abid, Beth Fabinsky, Larry Naes & Chao-Wei Tsai. *The Wide-field Infrared Survey Explorer (WISE): Mission Description and Initial On-orbit Performance.* *aj*, vol. 140, no. 6, pages 1868–1881, December 2010.

[Zonca 19]

Andrea Zonca, Leo Singer, Daniel Lenz, Martin Reinecke, Cyrille Rosset, Eric Hivon & Krzysztof Gorski. *healpy: equal area pixelization and spherical harmonics transforms for data on the sphere in Python.* Journal of Open Source Software, vol. 4, no. 35, page 1298, March 2019.